Inorganic Phototropism: Emergent Properties Directing Growth of Mesostructured Semiconductors

Thesis by

Madeline Claire Meier

In Partial Fulfillment of the Requirements
for the Degree of
Doctor of Philosophy

Caltech

CALIFORNIA INSTITUTE OF TECHNOLOGY
Pasadena, California

2023
(Defended April 24, 2023)

© 2023

Madeline Claire Meier
ORCID: 0000-0003-1608-0810

ACKNOWLEDGEMENTS

The act of getting a PhD is something that cannot be attributed to any one person alone. So many friends, family, and mentors have led me to and helped me through this experience, and I cannot begin to express my gratitude for all of their help before and throughout this process.

First of all I want to thank my advisor Professor Nathan Lewis. The Lewis group is such a remarkable place to learn and do research in large part to the environment that he cultivates. The collaborative and welcoming atmosphere is one of the main reasons I was interested in joining the group. I appreciate everything I have learned for Nate, in particular the importance of scientific communication and last but certainly not least, our shared love of Dodgers baseball.

I want to thank my committee members Harry Gray, Kathy Faber, and Geoff Blake for their scientific feedback and advice throughout this process. Furthermore, I wish to thank them for their support relating to career and job opportunities.

Barbara Miralles is the reason the Lewis group functions, and she consistently goes above and beyond for all of us. She is a constant source of joy, always available to help, and I will miss her dearly. Bruce Brunschwig, thank you for your help running the MMRC, instrumentation expertise, and constant supply of helpful research insights. Thank you to Kimberly Papadantonakis for all the support and mentorship during this process.

My experience with scientific research started as an undergrad at the University of Arkansas. I want to thank my advisor David Paul and Julie Stenken for all their encouragement to pursue graduate school and helpful advice along the way. Rob Coridan

was a postdoc for Nate and came to Arkansas during my time as an undergrad and I appreciate his insight into navigating grad school and life in the Lewis group.

The Lewis group is comprised of so many caring and unique individuals that have made this process more fun than it had any right to be: Matthias Ricther, Carlos Read, Miguel Cabán-Acevedo, Burt Simpson, Renata Balgley, Jingjing Jiang, Xinghao Zhou, Dan Torelli, Michael Lichterman, Jonathan Thompson, Azhar Carim, Stefan Omelchenko, Sisir Yalamanchili, Annelise Thompson, Paul Nuñez, Ivan Moreno Hernandez, Ellen Yan, Ethan Simonoff, Paul Kempler, Kat Rinaldi, Kyra Lee, Pai Buabthong, Katie Chen, Weilai Yu, Kathleen Kennedy, Harold Fu, Michael Mazza, Katie Hamann, Zach Ifkovits, Mo Morla, Jackie Dowling, Sean Byrne, Jake Evans, Alex Ye, Natasha Reich, and Dominic Covelli. Annelise Thompson was my first mentor at Caltech and taught me so much about the research process and the importance of protecting samples from Noyes dust.

The squigz subgroup is the best, and not just because of all the fun shapes we get to make. Azhar Carim has worn many hats throughout my time in graduate school. Azhar taught me so much of what I know about squiggles and the best places to get coffee and soft pretzels in the Pasadena area. His ability to weave together and write scientific stories is something I greatly admire. Katie Hamann and I often got mistaken for each other on Caltech's campus, and while neither of us fully understood why, being compared to Katie is a great compliment I was always happy to receive. Katie is such a caring and kind person with a dedication to research. We've gone through many journeys together inside the lab and out whether it be determining the best use of a Dremel or trying new pasta recipes. Jonathan and Ethan brought so much knowledge and fun to squigz and presented us with the wonderful gift of Conchorse. Sean has been an excellent addition to the squigz team and ace pitcher for Cold Fusion. I'm

so lucky that Sarah Kabboul was interested in doing summer research with the group. Sarah is the best undergraduate mentee I could have ever asked for and is always willing to go above and beyond for research even if that means enduring summer solstice heat for solar squigz deposition. Natasha Reich and I first met through our involvement with SEAL and I'm so glad she joined the group and is working on squiggles. She brings and infectious energy to the group and I truly am grateful for so many things including our frequent dance breaks in the office, consumption of endless amounts of cheese and crackers, and her friendship.

I have been fortunate enough to have a great support system throughout my time in graduate school in large part due to my wonderful family and friends. Evan and I met in high school but our friendship really grew while in undergrad even though we attended separate schools. Britney and Elizabeth are two of the most caring and thoughtful people I have ever met. Our monthly facetime sessions always remind me I am so fortunate to have met you both in college. Elizabeth Littlefield, Zach Ifkovits, Haley Bauser, and Michael Mazza provided support during a much needed time in COVID and well beyond through Zoom movie nights, pool days, trips to the mountains and desert, and so much more. To my family, thank you for all your support during this process and so much more. My parents are both teachers and have always placed great value on the importance of learning which inspired me from a young age. Their constant love and support has been instrumental in this process.

To Christian (and Winnie). Words cannot truly express how I feel. Everything I have achieved during this process has been because of your love and support. You are so talented,

smart, kind, and caring. You truly make every day better and I am so happy with the life

we've built together. This PhD would not have been possible without you.

ABSTRACT

Nature exhibits emergent growth phenomena where in neighboring features result in ensemble effects that direct the overall growth morphologies. Plants, such as palm trees, display phototropism where-in the crown grows toward the time weighted average position of the sun to optimize solar collection. A methodology, known as inorganic phototropic growth, utilizes a similar mechanism with the incident illumination during electrochemical deposition directing the growth of mesostructured semiconductors. This photoelectrochemical deposition process, generates highly anisotropic, periodic lamellar features resulting in the capability to fabricate nanostructured features over macroscopic areas. The process is lithography-free and uses no templates or directing agents of any kind and relies solely on the incident illumination to direct semiconductor growth. In this thesis, the nanophotonic phenomena and emergent synergistic absorption that drives the inorganic phototropic growth process was investigated using unconstrained and confined susbtrates. Additionally, the impact of inclined, off-normal incident illumination on the evolution of structure morphology was investigated for patterned and isotropic substrates revealing the mechanism behind the non-monotonic relationship between incident angle and observed out-of-plane orientation for unconstrained substrates.

PUBLISHED CONTENT AND CONTRIBUTIONS

Portions of this thesis have been drawn from the following publications:

Meier, M. C.; Cheng, W.-H.; Atwater, H. A.; Lewis, N. S.; Carim, A. I. Inorganic Phototropism in Electrodeposition of Se–Te. J. Am. Chem. Soc. 2019, 141 (47), 18658–18661. https://doi.org/10.1021/jacs.9b10579.
   M.C.M. performed the experiments and modeling, analyzed the data, and helped prepare the manuscript.

Meier, M. C.*; Carim, A. I.*; Kennedy, K. M.; Richter, M. H.; Hamann, K. R.; Lewis, N. S. Assessing Effects of Near-Field Synergistic Light Absorption on Ordered Inorganic Phototropic Growth. *J. Am. Chem. Soc.* **2021**, *143* (10), 3693–3696. https://doi.org/10.1021/jacs.0c13085.
   M.C.M. performed the modeling, analyzed the data, and helped prepare the manuscript.
   (*equal author contributions)

Meier, M.C.; Cheng, W.-H.; Richter, M. H.; Thompson, J.R.; Batara, N.T.; Yalmanchili, S.; Atwater, H. A.; Lewis, N. S.; Carim, A. I. Emergent Growth of Biomimetic Mesostructures via Inorganic Phototropism. *In Preparation.*
   M.C.M. performed the modeling and experiments, analyzed the data, and helped prepare the manuscript.

Meier, M.C.; Lewis, N. S.; Carim, A. I. Inclination of Polarized Illumination Increases Symmetry of Structures Grown via Inorganic Phototropism. *In Preparation.*
   M.C.M. performed the modeling and experiments, analyzed the data, and helped prepare the manuscript.

TABLE OF CONTENTS

LIST OF FIGURES

Chapter 1

INTRODUCTION AND BACKGROUND

1.1 Background

Many organisms in nature have evolved to exhibit complex mesostructured interfaces or growth properties with advantageous properties.[1–4] Lotus leaves demonstrate self-cleaning and water-wicking properties as a result of hierarchical microstructure mounds with additional nanoscale features.[2] Gecko feet present a multiscale structures that creates a superhydrophobic surface and improved adhesive force towards water.[3] In particular, manipulation of light to direct optical responses is a common feature of natural mesostructured systems.[5–7] Mesostructured features on the wings of butterflies, birds, and beetles result in vibrant, brilliant coloring through the nanostructures diffracting and reflecting light.[5,8,9] Beyond manipulation of light and optical properties through utilizing mesostructures, many organisms and species in nature use illumination to guide overall growth and morphology response.[10] Sunflowers adjust leaf orientation over the course of the day in a phenomenon known as heliotropism.[11] Many photosynthetic plants, e.g. cotton and bean, exhibit this type of movement as well as several other organisms including flies and small crustaceans.[12–16] Phototropism, a similar but distinct phenomenon from heliotropism, is defined as the growth in response to incident illumination. In some species of finger coral (Acropora pulchra), the growth and formation of new corrallites is directed towards light with the magnitude of the directing response increasing at shorter wavelengths.[17,18] Palm trees, such as those displayed in Figure 1.1a, tilt as a consequence

of the time-weighted average position of the solar azimuth in this case tilting south towards the equator as the trees are located in the northern hemisphere.[19] This process can be used the direct the growth of plant species such as the example present in Figure 1.1b, where-in the plant growth and thus orientation is off-normal towards the lamp illumination source.
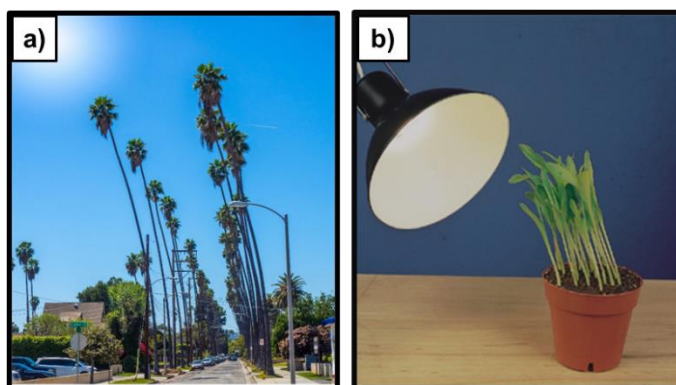
Figure 1.1. (a) Image of palm trees taken in Pasadena, California tilt towards the south due to phototropism. (b) Phototropism exhibited in planted seedlings that grow out from the soil towards the lamp illumination source.

Mimicking these advantageous structural features and phenomena is a highly active area of research for example, developing materials with structural color for anticounterfeiting applications inspired by the brilliant, iridescent colors present in butterflies and beetles, and generating water-wicking materials for solar evaporation systems based on lotus leaf architectures.[1,20] Substantial effort has been directed towards the generation of biomimetic photoactuators that exhibit a heliotropic response, for uses that include solar tracking for energy applications, remote triggering of chemical reactions, and construction of soft robots.[21–24] A recently discovered methodology, inorganic phototropic growth, investigated if the natural phenomena of phototropism could be extended to

inorganic materials to generate complex, nanoscale features without lithographic processes.[25–32]

1.2 Inorganic Phototropic Growth

In inorganic phototropic growth, electrochemical deposition is used in tandem with incident illumination to grow thin, nanostructured films of Se-Te as outlined in Figure 1.2.[25–28] The deposition process is lithography-free and utilizes no templates or directing agents but instead relies solely on the incident illumination to direct the morphology of the resulting mesoscale features. The reductive electrodeposition process takes place at room temperature in an aqueous solution consisting of 0.020 M SeO_2, 0.010 M TeO_2, and 2.0 M H_2SO_4.[33–35] If this process is done without illumination, no distinct features or anisotropy is observed as indicated in the scanning electron micrograph (SEM) presented in Figure 1.2b. In contrast, under illumination with a light-emitting diode (LED), an anisotropic, periodic lamellar pattern is formed (Figure 1.2c). This technique allows for the generation of nanoscale features conformally over cm^2 areas.
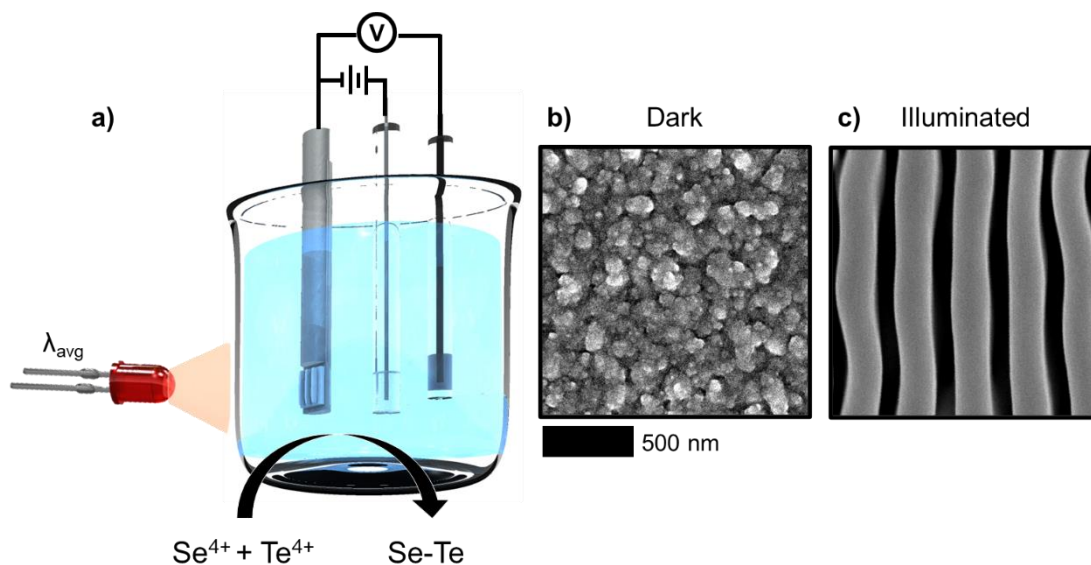
Figure 1.2. (a) Schematic illustrating inorganic phototropic growth via cathodic electrochemical deposition of Se-Te. (b) and (c) Representative SEM of Se-Te films deposited in the dark and using vertically polarized λ_{avg} = 727 nm illumination.

The resulting growth is hypothesized to originate from a difference in the growth rate in the dark versus under illumination. Figure 1.3 presents current density plotted as a function of time.[28] In the chopped light chronoamperomogram shown in Figure 1.3a, when the light is chopped, or turned off, the current is substantially less than when the substrate is illuminated. Optical modeling using point dipole radiation sources can be used to simulate the electric field intensity at the growth interface. Figure 1.3b displays two dipole emitter sources, in a medium with the same refractive index as the deposition solution, oriented in the same propagation axis as vertically linearly polarized illumination spaced two wavelengths apart.[27] The electric field observed is an oscillatory pattern with regions of high and low intensity. In the chopped light choronoamperogram data (Figure 1.3a), areas with greater illumination will exhibit higher growth rates, and therefore this oscillatory intensity profile results in oscillatory mass addition across the substrate.
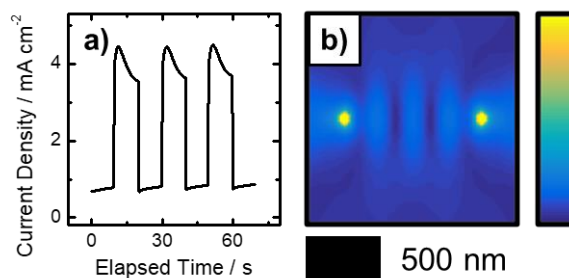
Figure 1.3. (a) Chopped light choronoamperomogram during the deposition of Se-Te thin films. (b) Optical modeling of the electric field with two dipole radiation sources emitting $\lambda_{avg} = 630$ nm, oriented vertically in a medium of n = 1.33.

Figure 1.4 presents and summarizes a simplified schematic of inorganic phototropic growth. The process starts with a conductive, planar substrate (Figure 1.4a) with initial randomly deposited Se-Te nucleation features (Figure 1.4b). As the incident illumination present throughout the growth process scatters off these features, areas of higher and lower intensity result due to constructive and destructive interference, respectively (Figure 1.4c) leading to preferential mass addition where local light absorption is highest (Figure 1.4d) creating a positive feedback loop that ultimately results in nanostructured feature formation (Figure 1.4e).
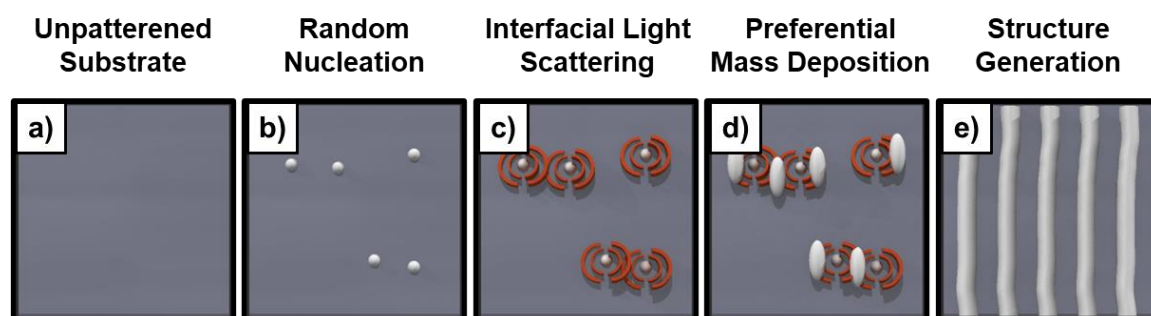
Figure 1.4. Schematic illustrating the inorganic phototropic growth process from the initial planar substrate through the final structure formation.

The inorganic phototropically grown thin films encode the optical illumination inputs utilized during the deposition process, and thus the morphology of the photoelectrochemical deposits generated via this methodology can be directed through changes in the incident illumination parameters including polarization and wavelength. Figure 1.5 displays the change in morphology induced from changes in the polarization of incident illumination. Unpolarized incident illumination results in a periodic mesh-like pattern forming across the substrate as displayed in the SEM in Figure 1.5a. Linearly polarized illumination generates highly anisotropic, periodic lamellar patterns (Figure 1.5b-d) with the long axis of the lamella features oriented parallel to the direction of polarization, consistent with the oscillatory pattern predicted from the dipole optical modeling in Figure 1.3b.[27] In addition to anisotropy from the top-down perspective, further investigation of the nanoscale feature morphology can be conducted through cross-sectional SEM analysis. Figure 1.5e,f present cross-sectional SEMs parallel and perpendicular to the incident polarization highlighting the out-of-plane anisotropy. In particular, the perpendicular cross section (Figure 1.5f) illustrates the high aspect ratio and growth of the features out from the substrate along the normal towards the incident illumination source.
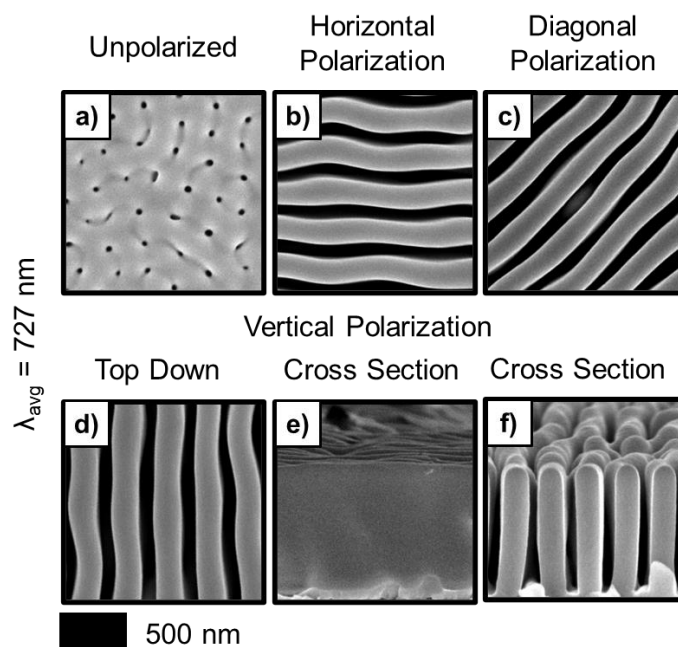
Figure 1.6. Representative top-down and perpendicular cross-sectional SEMs of photoelectrochemical deposits using the indicated wavelengths.

The reasoning behind these trends can be explored through an optically based growth model illustrated in Figure 1.7. This two-step iterative growth model contains few empirical inputs, only estimates of the electrolyte index and deposit complex refractive index.[28,36] In the first step, full-wave electromagnetic simulations are performed using a finite-difference time-domain (FDTD) method to calculate the local light absorption in the system. Then mass is added via a Monte Carlo method wherein mass is added probabilistically based on the local light absorption.
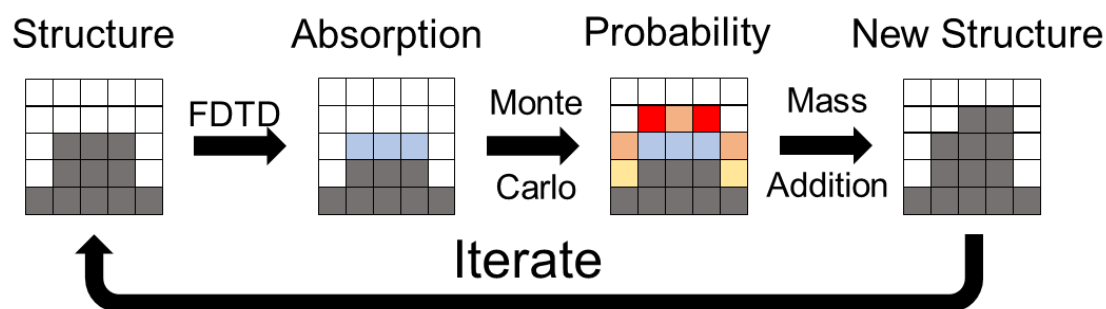
Figure 1.7. Schematic of the two-step optically based growth model where the first step calculates local light absorption that then informs a probabilistic mass addition step. This process iterates to mimic the inorganic phototropic growth process.

A series of iterations using this optically based growth model and the final resulting simulated morphology produced using this simulation method is presented in Figure 1.8. The start of the simulated growth process consists of a planar substrate with no templating or lithographically patterned features of any kind (Figure 1.8a). Mass is then added iteratively with initial random deposits (Figure 1.8b) evolving via a positive feedback loop to generate light-directed preferential mass addition (Figure 1.8c,d) that ultimately converges to the anisotropic lamellar morphology observed experimentally (Figure 1.8e). The agreement between the growth model simulated structures and those produced experimentally reinforces the hypothesis that inorganic phototropic growth is an optical directed phenomena as the growth model contains only optically-based empirical inputs.

Optically Based Growth Model
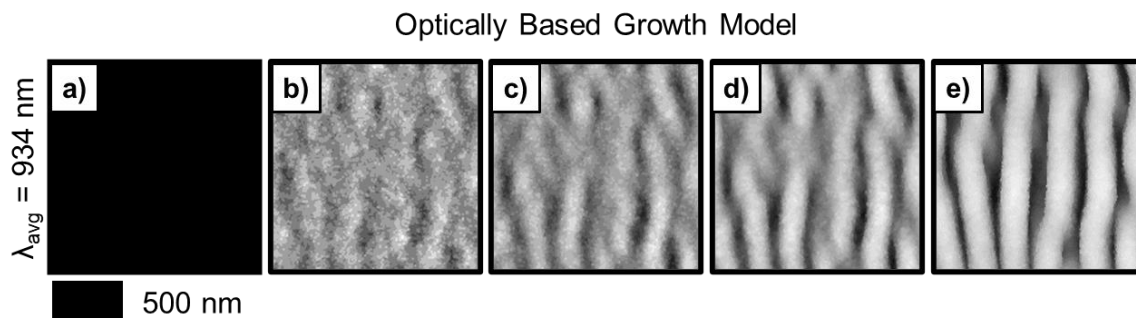
Figure 1.8. Increasing iterations of simulated structures generated via the two-step, opticall- based growth model at $\lambda_{avg} = 934$ nm.

Additional growth modeling of other material systems indicated that inorganic phototropic growth is not limited to solely Se-Te thin films. Specifically, Se-Pb (Figure 1.9) and Se-Cd (Figure 1.10) were investigated and found to generate similar lamellar morphologies both computationally and experimentally.[37,38] The fabrication of complex structures of multiple materials through modeling and laboratory methods indicates that the inorganic phototropic growth methodology can be generalizable to all semiconducting systems with sufficient photoactivity and capability of being deposited via electrochemical methods. Further material discovery is an ongoing research area within inorganic phototropic growth research.
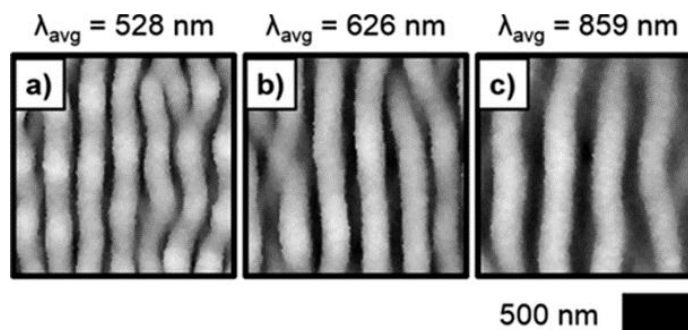
Figure 1.9. Simulated morphologies of Se-Pb films generated by inorganic phototropic growth using vertically polarized illumination with the indicated λ_{avg}.
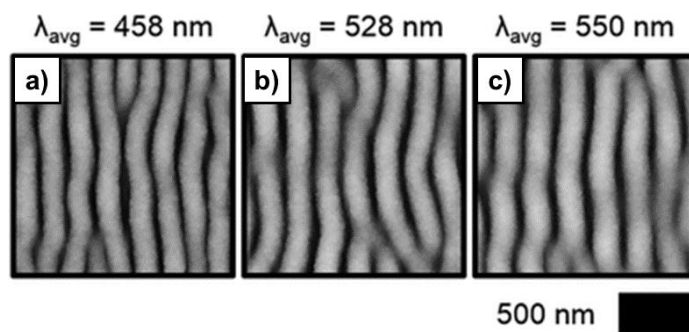
Figure 1.10. Simulated morphologies of Se-Cb films generated by inorganic phototropic growth using vertically polarized illumination with the indicated $\lambda_{avg.}$

1.3 Scope of Thesis

The subsequent thesis chapters build upon previous investigations into inorganic phototropic growth. Chapter 2 studies the intrinsic phototropism in Se-Te material systems with no optical communication or ensemble phenomena between deposition sites using normal and inclined incident illumination. Chapter 3 examines the emergent, nanophotonic properties that drive the inorganic phototropic growth process and the length scale of these interactions. Chapter 4 explores the impact of inclined illumination for films in communication, the emergent optical properties that generate the tilted photoelectrodeposited features, and the similarities between inorganic and biological systems. Chapter 5 investigates the improved fidelity of photoelectrodeposited features generated with inclined illumination in the same plane as incident polarization.

INORGANIC PHOTOTROPISM IN ELECTRODEPOSITION OF SE–TE

2.1 Introduction

Photoelectrochemical deposition of Se–Te on isolated Au islands using an unstructured, incoherent beam of light produces growth of Se–Te alloy toward the direction of the incident light beam. Full-wave electromagnetic simulations of light absorption indicated that the induced spatial growth anisotropy was a function of asymmetric absorption in the evolving deposit. Inorganic phototropic growth is analogous to biological systems such as palm trees that exhibit phototropic growth wherein physical extension of the plant guides the crown toward the time-averaged position of the sun, to maximize solar harvesting.

2.2 Results and Discussion

Se–Te was electrochemically grown under illumination on circular Au islands that were lithographically patterned onto an n+-Si substrate. The feature size and pitch of the Au islands were designed to minimize optical and electrochemical communication between adjacent regions of growth. Such isolation enabled investigation of the intrinsic material growth behavior independent of emergent phenomena, including array effects, which may dominate the growth characteristics of an unconstrained, extended film.[28] Figure 2.1a-c presents representative cross-sectional scanning-electron micrographs (SEMs) of isolated Se–Te deposits generated using a narrowband light-emitting diode (LED) source with an intensity-weighted average wavelength, λ_{avg}, of 528 nm, with the illumination incident at the indicated angle, α, from the surface normal. With α = 0° (normal incidence, Figure 2.1a), a symmetrical, hemispherical cross-section was observed. For α = 30° (Figure 2.1b) the deposit cross-section was mostly hemispherical, but exhibited some asymmetry in that greater mass was observed on the side of the incident illumination relative to the opposite side. For α = 60° (Figure 2.1c), a larger growth anisotropy was observed than for α = 30° (Figure 2.1b). Figure 2.1d-f present top-down SEMs analogous to the cross sections presented in Figure 2.1a-c. With α = 0° (Figure 2.1d), the deposit morphology was symmetrical, with an apparent circular projection. For both α = 30° and α = 60° (Figure 2.1e,f) less mass addition, and increased apparent roughness, was observed on the far side of the deposits, away from the direction of incident illumination. Hence the growth of Se–Te deposits can be directed to mimic the natural phototropism observed in biological

systems, wherein mass addition is directed asymmetrically to extend the structure along the path of the incident illumination.
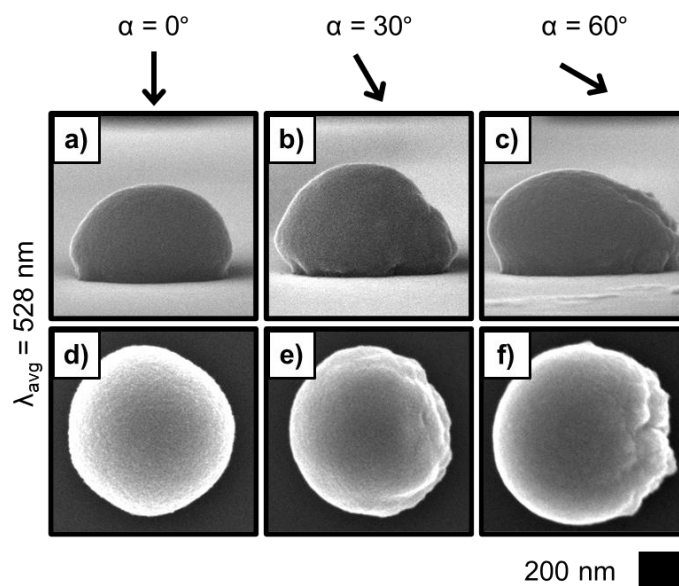
Figure 2.1. (a–c) Cross-sectional and (d–f) top-down SEMs representative of photoelectrodeposits generated with λavg = 528 nm illumination incident at the indicated angle α from the substrate normal.

In many plant systems that exhibit phototropic growth, including the model organism Arabidopsis, the magnitude of the natural phototropic response is a function of the illumination wavelength, with phototropic growth primarily observed in response to photosynthesis stimulated by short-wavelength visible light.[10,39] The mechanism of natural phototropic growth has been explained by the molecular absorption necessary to drive the photochemical reactions that underpin the biological growth response, in conjunction with an auxin-related response that causes cells to elongate at locations farthest from the light. [40–42] Herein, electrochemical growth using illumination sources with several λ_{avg} values was investigated to explore the wavelength sensitivity of Se–Te inorganic phototropic growth. Figure 2.2a–c presents cross-sectional SEMs of deposits generated using a LED

with λ_{avg} = 727 nm with varying values of α. With α = 0° (Figure 2.2a) a symmetrical, hemispherical cross-section was observed, similar to the case of normally incident λ_{avg} = 528 nm illumination (Figure 2.1a). For α = 30° (Figure 2.2b), some azimuthal asymmetry was observed in the deposits, with increased mass addition on the side of the incident illumination, but with less azimuthal asymmetry than growth using λ_{avg} = 528 nm at α = 30° (Figure 2.1b). The deposit generated with α = 60° (Figure 2.2c) exhibited the same type of asymmetry as for α = 30° (Figure 2.2b) but with substantially greater azimuthal asymmetry, similar to the case of λ_{avg} = 528 nm incident at α = 60° (Figure 2.1c). Figure 2.2d–f presents data analogous to that presented in Figure 2.2a–c, but for deposits generated using a LED with λ_{avg} = 843 nm. In all three cases (α = 0, 30, and 60°) a symmetrical, hemispherical cross-section was observed. Similar to the behavior observed in natural systems, the magnitude of the inorganic phototropic response varied with wavelength, and asymmetry was not observable for growth stimulated by illumination having a sufficiently long wavelength (near-infrared).
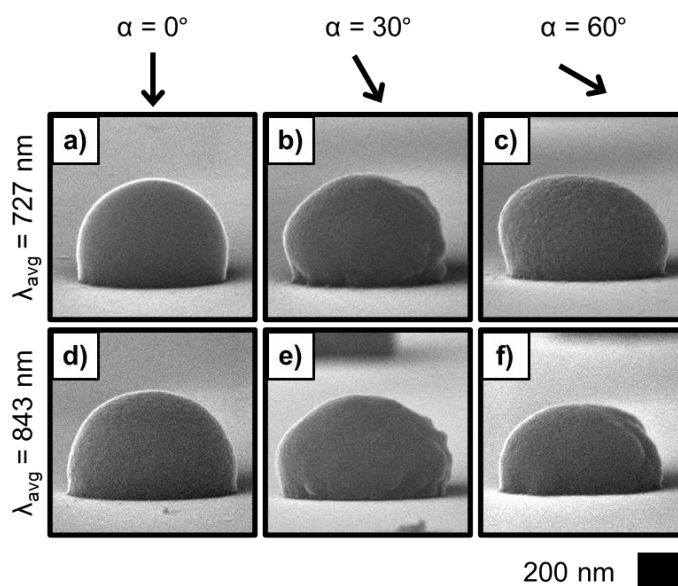
Figure 2.2. Cross-sectional SEMs representative of photoelectrodeposits generated with the indicated λ_{avg} illumination incident at the indicated angle α from the substrate normal.

To gain insight into the relation between the material absorption and the observed phototropic response, light absorption simulations were performed using full-wave electromagnetic simulations.[43] Model Se–Te structures about metallic islands in an electrolyte solution were used as representations of the morphologies that developed during photoelectrochemical growth. Analysis by energy-dispersive X-ray (EDX) spectroscopy and Raman spectroscopy (Figure 2.3) indicated that the composition of the photoelectrodeposited material was independent of the illumination inputs for the investigated parameter space.
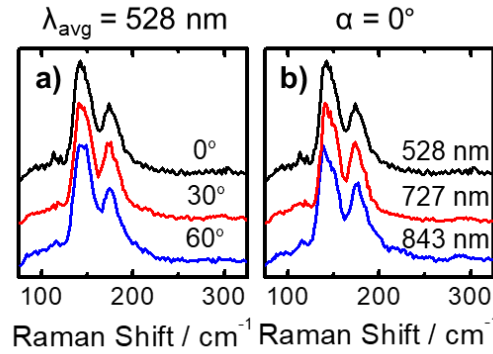
Figure 2.3. Representative Raman spectra of photoelectrodeposits generated with (a) λavg = 528 nm illumination incident at the labeled angle α from the substrate normal and (b) with the labeled λavg illumination incident at α = 0° from the substrate normal.

The simulation set up is depicted in Figure 2.4 and the materials properties used in the modeling were in accord with the composition of the material measured experimentally by EDX and Raman spectroscopies. The optical extinction coefficient of Se–Te alloys decreases with increasing wavelength from the visible regime to the near-infrared regime.[44] Figure 2.5a–c presents graphical representations of the light absorption profiles calculated for the model structure using λ_{avg} = 528 nm for α = 0, 30, and 60°. For α = 0° (Figure 2.5a), the absorption profile was symmetrical and most of the absorption was strongly localized near the growth (solution) interface. With α = 30° (Figure 2.5b), the absorption was also tightly confined near the solution interface but was asymmetrically distributed spatially, with greater absorption on the side of the incident illumination. A similar profile, but with a greater degree of angular asymmetry, was observed for α = 60° (Figure 2.5c). The extent of asymmetry in the absorption profiles correlated with the morphological anisotropies observed for deposits generated with the λ_{avg} = 528 nm source (Figure 2.1). The greater surface roughness observed for deposits generated with the λ_{avg} = 528 nm source and α = 30 and 60° (Figure 2.1e,f) on the far side, away from the direction of illumination

incidence, relative to the illuminated side, is similar to the roughness observed for a deposit generated in the dark (Figure 2.6). This observation suggests that the absorption of light by the deposit is sufficient to attenuate light-directed growth on the far side and relatively favor dark growth wherein mass addition may be dictated by electrochemical kinetics.
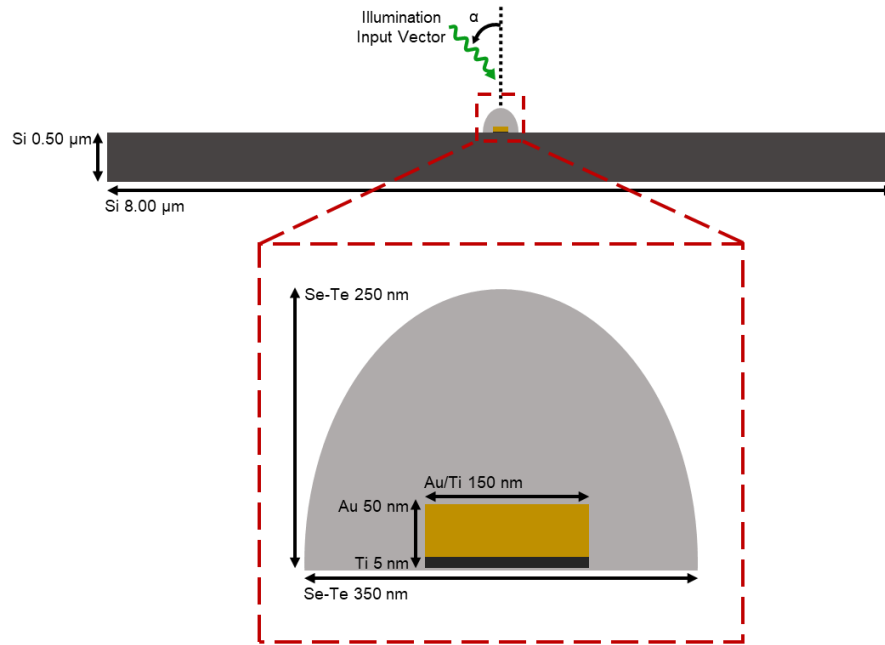
Figure 2.4. Schematic of the geometry utilized for light absorption modeling with idealized photoelectrodeposit structures.

Figure 2.5d–f present data analogous to that shown in Figure 2.5a–c but for calculations using $\lambda_{avg} = 727$ nm. For $\alpha = 0°$ (Figure 2.5d), the profile was symmetric but exhibited less concentration of absorption along the solution interface than for $\lambda_{avg} = 528$ nm (Figure 2.5a). For $\alpha = 30°$ (Figure 2.5e) the profile showed some absorption concentration on the side of the incident illumination but was more azimuthally isotropic than the profile for $\lambda_{avg} = 528$ nm with $\alpha = 30°$ (Figure 2.5b). With $\alpha = 60°$ (Figure 2.5f), the absorption was asymmetrically concentrated on the same side of the normal as the incident illumination but was not confined as strongly along the interface as for any angle of incidence with $\lambda_{avg} = 528$ nm (Figure 2.5a–c). The decreased optical concentration near the growth interface observed in the profiles for $\lambda_{avg} = 727$ nm relative to those for $\lambda_{avg} = 528$ nm is consistent with the decrease in extinction coefficient of the Se–Te material as the wavelength increases. As for $\lambda_{avg} = 528$ nm, the azimuthal symmetry observed in the

absorption profiles for λ_{avg} = 727 nm (Figure 2.5d–f) is consistent with the morphological anisotropy in the deposits generated with the same λ_{avg} (Figure 2.2a–c).

Figure 2.5g–i presents representations of absorption profiles similar to those presented in parts a–c and d–f of Figure 2.5, but for calculations using λ_{avg} = 843 nm. For α = 0° (Figure 2.5g) the profile is symmetric, but a similar magnitude of absorption is observed in both the apex of the structure near the solution interface and at the bottom of the structure near the substrate interface, in contrast to the profile observed for λ_{avg} = 528 nm with α = 0° (Figure 2.5a). For α = 30° and 60° (Figure 2.5h,i), some azimuthal asymmetry in the absorption profiles was observed, with the absorption biased toward the side of the incident illumination. However, the overall localization of the absorption was lower than observed in the analogous cases with λ_{avg} = 727 nm (Figure 2.5e,f). The low degree of optical concentration observed in the profiles for λ_{avg} = 843 nm (Figure 2.5g–i) is consistent with the lower material optical absorption at this wavelength than at λ_{avg} = 528 nm or λ_{avg} = 727 nm, and is moreover consistent with the lack of morphological anisotropy observed experimentally for deposits generated with the λ_{avg} = 843 nm source. The computational data, in conjunction with experimental results, thus indicates that the phototropic response arises from spatially anisotropic absorption in the growing deposits, which in turn promotes locally elevated rates of electrochemical growth where absorption is high, resulting in directional growth.[27,43] A phototropic response was not observed when the optical absorption was predominantly spatially isotropic, such as for λ_{avg} = 843 nm (Figure 2.5g–i). Due to low optical absorption and thus high optical penetration under these

conditions, the isotropic absorption resulted in spatially isotropic rates of mass addition along the growth interface, effecting symmetric deposits.
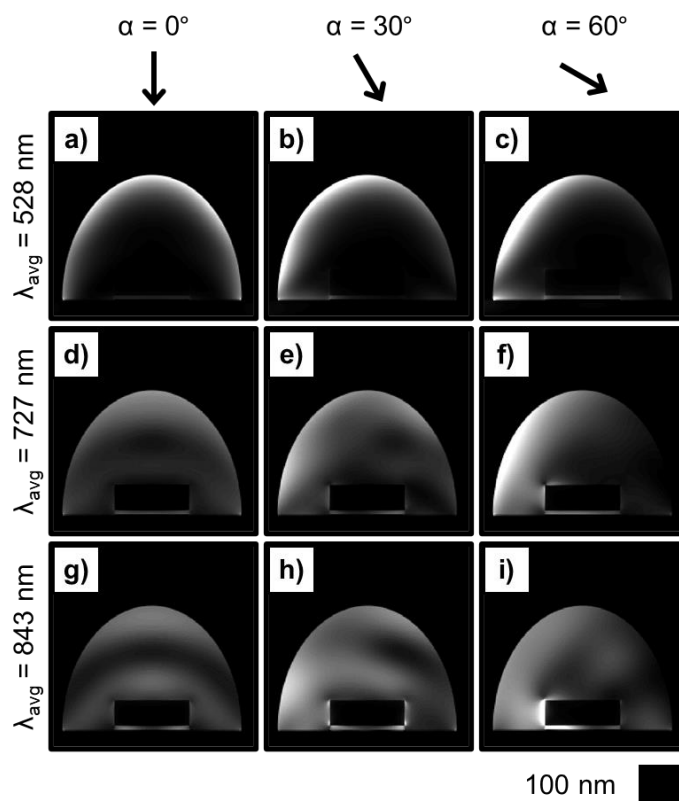
Figure 2.5. Simulated light absorption profiles in a model photoelectrodeposit morphology for illumination with the indicated λ_{avg} incident at the indicated angle α from the substrate normal.
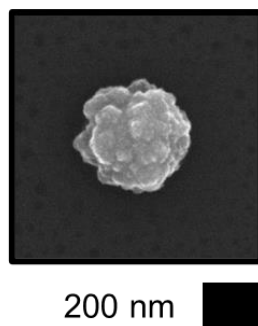
Figure 2.6. Top-down SEM representative of a deposit generated in the dark.

2.3 Conclusions

The cumulative data presented herein demonstrate that inorganic phototropic growth, wherein material addition is directed toward an unstructured light beam in free space in analogy to the manner that many plants grow toward the sun, can be achieved via light-guided electrochemical growth of Se–Te. The directionality of the inorganic phototropic response is a function of direction of the illumination incidence whereas the magnitude of the response is dependent on both the incidence vector and the wavelength. Simulations of light absorption in model Se–Te deposits, combined with the experimental data, indicate that the phototropic response is a consequence of spatially anisotropic absorption in the evolving material. Techniques to capitalize on inorganic phototropic response to construct complex three-dimensional morphologies that may be difficult or impossible to generate via conventional lithographic means are now being investigated.

ASSESSING EFFECTS OF NEAR-FIELD SYNERGISTIC LIGHT ABSORPTION ON ORDERED INORGANIC PHOTOTROPIC GROWTH

3.1 Introduction

We report herein that synergistic light absorption in the optical near-field enables nanoscale self-organization during inorganic phototropic growth. Se–Te was grown electrochemically under illumination from an incoherent, unstructured light source in geometrically constrained, wavelength scale areas. Despite the limited dimensions, with as few as two discrete features produced in a single sub-micron dimension, the deposit morphology exhibited defined order and anisotropy. Computer modeling analysis of light absorption in simulated structures revealed a synergy wherein light capture in a nanoscale feature was enhanced by the presence of additional adjacent features, with the synergistic effect originating predominantly from nearest-neighbor contributions. Modeling moreover indicated that synergistic absorption is produced by scattering of the incident illumination by individual nanoscale features, leading to a local increase in the near-field intensity and consequently increasing the absorption in neighboring features. The interplay between these optical processes establishes the basis for spontaneous order generation via inorganic phototropic growth.

3.2 Results and Discussion
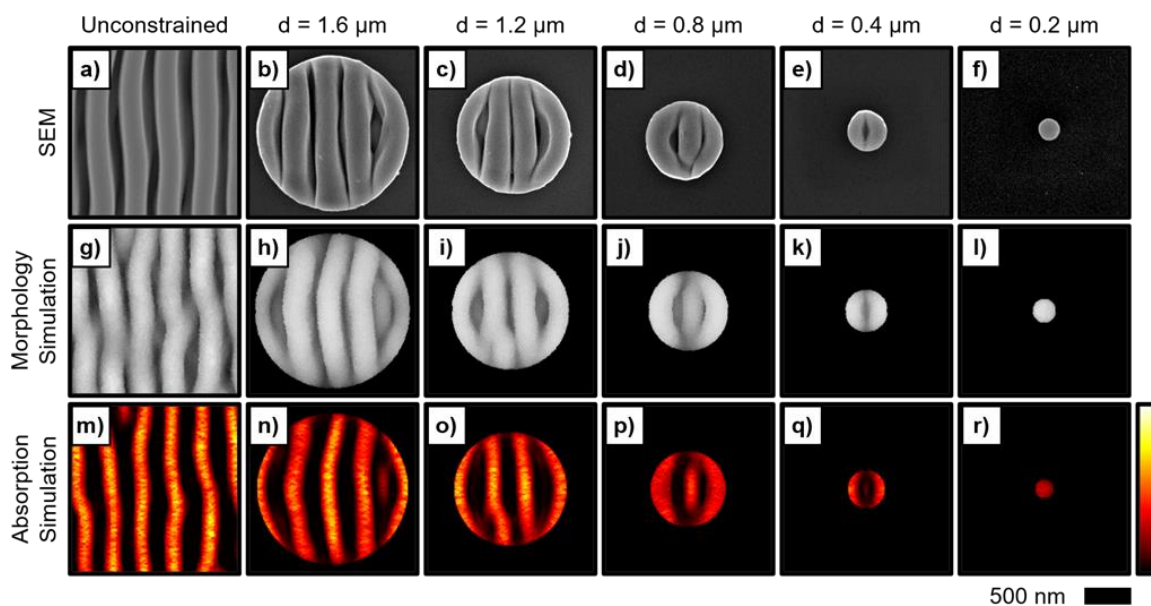
Figure 3.1. Representative SEMs of experimentally generated Se–Te deposits, grown from a solution of 0.0200 M SeO2, 0.0100 M TeO2, and 2.00 M H2SO4 using vertically polarized λavg = 934 nm illumination, without spatial constraint (a) and with areal constraint to the indicated circular diameter (b–f). Computer simulations of deposit morphologies generated via modeling of the growth (g–l) analogous to the empirical data in the above row. Light absorption profiles (m–r) corresponding to the simulated morphologies in the above row.

The impact of physically confined growth on Se-Te nanostructures was studied to understand the short-range, optical communication among neighboring nanoscale features. Figure 1a presents a representative scanning-electron micrograph (SEM) of a Se–Te deposit generated via inorganic phototropic growth on a planar, unpatterned, substrate. The deposit exhibited a highly anisotropic and ordered morphology consisting of vertically oriented lamellar features, in accord with prior work showing that on conductive, non-photoactive substrates (e.g., n+-Si, Au) template-free growth of Se–Te, as well as Se–Pb and Se–Cd, can spontaneously generate periodic structures oriented along an arbitrarily selected incident optical polarization direction.[26,37,38] Here, inorganic phototropic growth

was effected by light-mediated electrochemical synthesis of Se–Te from a solution of 0.0200 M SeO_2, 0.0100 M TeO_2, and 2.00 M H_2SO_4 using vertically polarized illumination with an intensity-weighted average wavelength (λ_{avg}) of 934 nm from an incoherent, narrowband light-emitting diode source. No photomask was used. In-plane growth was then confined to dimensions that were comparable to the wavelength of the incident illumination by using substrates coated with a nonconductive poly(methyl methacrylate) (PMMA) layer in which circular well structures had been defined via electron-beam lithography. Growth proceeds via the light-stimulated electrochemical deposition process and cannot occur on regions of the substrate coated with an electrically insulating film such as PMMA. The well geometries did not limit mass transport between the bulk solution and the growth interface and did not influence the morphologies beyond the effect of lateral confinement. The concentration of precursor species is sufficiently large such that mass transport is not outpaced by the photodriven electrochemical deposition. The circular geometry prevented the relative alignment of the optical polarization and the PMMA structures from affecting the growth (as would be possible with an anisotropic confinement geometry). Figure 3.1b–f presents representative SEMs of deposits generated with spatial confinement of the indicated circular diameter, d. With d = 1.6 μm (Figure 3.1b), a lamellar morphology was observed and consisted of five vertically oriented features. These features are very similar to those observed for inorganic phototropic growth on unpatterned large scale (cm^2 area) substrates (Figure 3.1a). The outermost feature on each side of the confined area exhibited curvature imposed by the circular confinement pattern. Relative to d = 1.6 μm (Figure 3.1b), growth confined to d = 1.2 μm (Figure 3.1c) resulted in a similar

morphology but consisted of two instead of three central features. Only a singular central feature was observed when d = 0.8 μm (Figure 3.1d), whereas for d = 0.4 μm (Figure 3.1e), a central feature was not produced and instead a vertically oriented central depression was bordered by a single feature on each side. When the growth area was constrained to d = 0.2 μm (Figure 3.1f), a single circular feature filled the growth region. These data demonstrate that inorganic phototropic growth, despite spatial confinement to wavelength scale dimensions and the consequent lack of any ensemble phenomena that may occur in an unconstrained case, can generate morphological order and anisotropy, even with as few as two discrete structural features.

Computer simulations were performed to explore the principles that enable inorganic phototropic growth to direct morphological anisotropy and order at the wavelength scale. A two-step iterative model with an optical basis was utilized to emulate the bottom-up growth process. First, an electromagnetic method was used to simulate illumination of the growth interface and calculate the magnitude of light absorbed at each point along the interface. Then, Se–Te mass was selectively added to the interface in a probabilistic fashion using a Monte Carlo method wherein the likelihood of mass addition at a certain location scaled with the local light absorption magnitude as determined in the previous step. These steps were successively iterated, with a new evaluation of the absorption in the evolved interface resulting from mass addition in the immediately previous iteration. This process has been shown to reproduce the structural genesis and evolution of films generated by inorganic phototropic growth.[29] Empirical inputs were minimal and included estimates of the deposit complex refractive index and the electrolyte

index. Figure 3.1g–l presents simulated morphologies analogous to the experimental observations depicted in Figure 3.1a–f. Each simulated morphology is the result of a discrete, independent set of growth computations initialized from an isotropic substrate. In all cases, the simulated morphology was in remarkable accord with that observed experimentally. Such agreement between the experimental and computational data indicates that the structures observed experimentally are determined by optical processes as opposed to a chemical or crystallographic bias of the Se–Te material or any other physical processes, for example, mass transport, during growth.[45–47]

Light absorption in the morphologies generated by the optically based growth modeling was evaluated to assess the basis for structure determination. Figure 3.1m–r presents the spatial profiles of light absorption derived from the growth modeling that correspond to the simulations displayed in Figure 3.1g–l, respectively. For a spatially unconfined film (Figure 3.1m), the intensity in the absorption profile closely tracked the simulated film morphology (Figure 3.1g), with relatively high absorption along all the observed lamellar features and minimal absorption in the space between the features. When growth was confined spatially to d = 1.6 μm (Figure 3.1n), the highest absorption intensity was observed along the centermost feature, with some elevated absorption in the neighboring features near the vertical midpoints. A similar absorption profile was observed for growth when the spatial confinement was constrained to d = 1.2 μm (Figure 3.1o), with the largest intensity at the middle of the central features. For d = 0.8 and 0.4 μm (Figure 3.1p,q), the absorption still tracked the principal growth features, but exhibited less contrast and was lower in magnitude than for d = 1.6 or 1.2 μm (Figure 3.1n,o). The lowest relative

absorption, with minimal spatial variance in the circular area, was observed for d = 0.2

µm (Figure 3.1r). These data indicate a synergistic nanophotonic phenomenon in which the

absorption in an individual feature is enhanced by the presence of additional adjacent

features. Notably, an absorption profile that was very similar to that of the spatially

unconfined growth (Figure 3.1m) was obtained with only four or five total parallel features

(Figure 3.1o,n). These data indicate that the synergistic absorption in an individual feature

is predominately determined by the contributions of the very nearest neighbors, suggesting

that the self-organization observed during inorganic phototropic growth is primarily

directed by short-range light-matter interactions within the optical near-field.
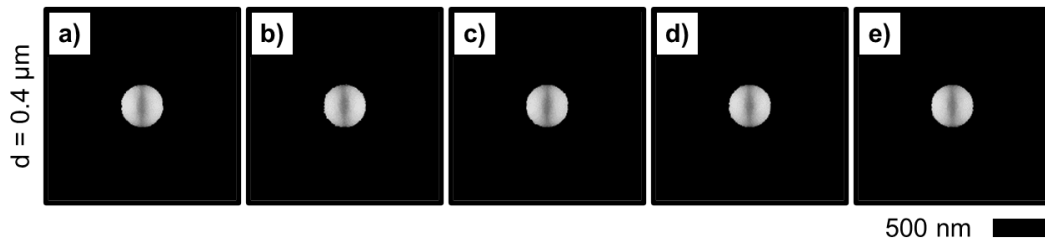
Figure 3.2. Simulated Se-Te deposit morphologies generated considering λavg= 934 nm illumination with areal constraint to the circular diameter d= 0.4 µm. Each panel presents the result of a fully independent set of growth computations.

Figure 3.2 presents simulated morphologies of Se-Te deposits generated from

independent sets of computations using the iterative, two-step growth model considering

λ_{avg} = 934 nmillumination with areal constraint to the circular diameter d = 0.4 µm. The

extremely close accord between these mutually independent simulations of bottom-up

mass addition compellingly indicates that the observed structures are a direct result of light-

matter interactions between the input illumination and the evolving Se-Te deposits.

Additional computational modeling was performed to further explore the optical interactions between neighboring deposit features and interrogate the length scale that is relevant and determinative of the emergent film growth evident in the experiments and simulations presented in Figure 3.1 for inorganic phototropic growth with circular spatial confinement. A simplified, idealized lamellar feature was designed with shape and dimensions characteristic of those observed experimentally. Morphologies with a single such feature, as well as one with two features separated by the feature pitch observed experimentally, were modeled and are presented schematically in Figure 3.3 a,b. Spatial confinement, as was effected using a substrate patterned with circular well structures for the experimental as well as computational growth modeling investigations (Figure 3.1), was not utilized here. The structures were explicitly predefined rather than generated spontaneously, but the experimental and simulated growth results demonstrated that analogous structures are generated spontaneously during inorganic phototropic film growth. Stimulation was simulated with the same illumination utilized both experimentally and in the growth modeling, and the spatial absorption profiles were calculated and are presented in Figure 3.3 c,d. Enhanced absorption was observed in the simulation that contained two features (Figure 3.3d) relative to that with the single feature (Figure 3.3c), consistent with the synergistic absorption phenomenon observed in the growth modeling data. Figure 3.3e presents a simulation of the spatial profile of the time-averaged electric field magnitude corresponding to the absorption data in Figure 3.3c. An enhancement in the amplitude of the field was observed in the regions directly adjacent to the lamellar feature. Figure 3.3f presents a simulation analogous to that in Figure 3.3e, but for the case

of two features (Figure 3.3b), and shows a similar enhancement in the regions adjacent to the outer edges of the features. These data indicate that the features anisotropically scatter the incident illumination, effecting optical localization and concentration in the immediate vicinity of the feature of concern. Synergistic absorption thus occurs when a neighboring feature is present. Such scattering and absorption processes in the optical near-field consequently provide the basis for spontaneously ordered inorganic phototropic growth. These results indicate that inorganic phototropic growth can direct the morphological anisotropy and order at spatial scales comparable to the incident optical wavelength, in the absence of any emergent ensemble phenomena that may result at longer extended length scales.
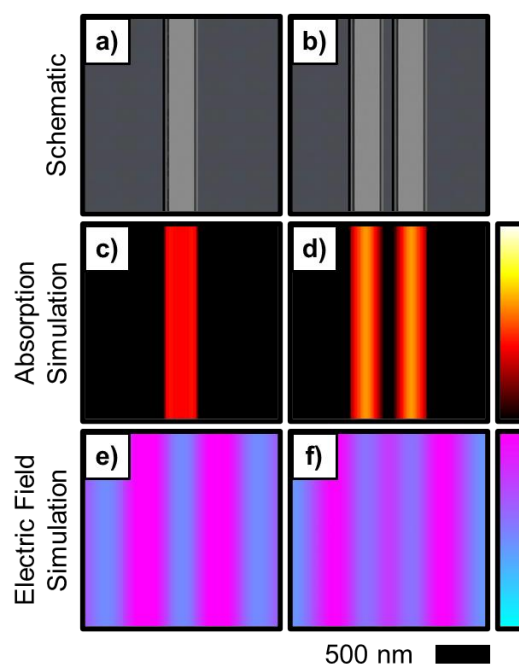
Figure 3.3. Schematic of simplified lamellar morphologies (a, b) and corresponding simulations of the light absorption (c, d) and time-averages of the electric field magnitude (e, f).

3.3 Conclusions

In summary, inorganic phototropic growth was performed over wavelength scale areas, and morphological anisotropy and order were observed in the deposits despite the limited length scale. The growth morphologies were simulated using a fully optically based model and were in close agreement with the experimental observations, indicating that the morphologies are primarily determined by optical phenomena. Light absorption in the simulated morphologies was analyzed, and synergy was observed in which absorption in a single feature was enhanced by the presence of adjacent, neighboring features. The features scattered the incident illumination, enhancing the relative intensity in the directly adjacent regions. This scattering process thus feeds the absorption synergy, establishing the nanophotonic basis that promotes cooperative growth and demonstrating that extended ensemble phenomena are not necessary to direct structure and produce spontaneous organization in inorganic phototropic growth.

Chapter 4

EMERGRENT GROWTH OF BIOMIMETIC MESOSTRUCTURES VIA INORGANIC PHOTOTROPISM

Meier, M.C.; Cheng, W.-H.; Richter, M. H.; Thompson, J.R.; Batara, N.T.; Yalmanchili, S.; Atwater, H. A.; Lewis, N. S.; Carim, A. I. Emergent Growth of Biomimetic Mesostructures via Inorganic Phototropism. *In Preparation.*

4.1 Introduction

We show that photoelectrodeposition of Se-Te using inclined illumination generates ordered nanoscale features oriented away from the substrate normal and consistently towards the local maximum in near-field intensity, and that this behavior is comparable to the light-directed habit formation of several tree species. Emergent, nanophotonic behavior effected apparent inorganic phototropic growth towards as well as skototropic growth away from, the far-field illumination vector, at different input inclination regimes. The collective data reveals a commonality between photoresponsive morphology determination in biological and inorganic systems and opens new avenues for the programmable fabrication of inorganic mesostructures with minimal time and material inputs in a scalable fashion.

4.2 Results and Discussion

Photoelectrodeposition of semiconducting Se-Te from aqueous solution on a substrate templated with optically-isolated conductive islands results in material growth towards the direction of the stimulating light beam.[48] Directional growth is a consequence of asymmetric light absorption in the deposit which effects spatially varying rates of photoelectrochemical mass addition. In analogy to natural phototropism, this light-directed deposition is termed inorganic phototropic growth. Maskless inorganic phototropic growth of Se-Te, as well as other semiconducting chalcogen alloys, using incoherent (uncorrelated) illumination inputs with spatially uniform intensity profiles on template-free substrates has been demonstrated to spontaneously generate highly ordered mesostructures over cm^2 areas, including anisotropic, three-dimensional lamellar morphologies.[28,37,38] Photoelectrodeposit morphologies are dictated by the characteristics of the illumination inputs utilized during growth, with the spectral distribution controlling the feature size and pitch, and the polarization defining the direction and associated magnitude of the anisotropy.[25–27] Time-varying optical inputs can produce further morphological intricacy, e.g. aqueduct and tuning fork morphologies.[29,30] Structure generation during inorganic phototropic growth in the absence of templating agents is a consequence of inherent asymmetries in the light-material interactions during deposition that shape the optical absorption profile at the growth interface.[36]

In this work, inorganic phototropic growth was performed on an isotropic substrate with the illumination incidence at a series of inclinations from the substrate normal. This assessment seeks to evaluate, quantify, and fundamentally understand the extent to which

photoelectrodeposition produces directed growth of mesostructured material toward, or away from, illumination with spatially uniform intensity. Ensemble effects in the extended structure may perturb the response to the inclined input similar to how trees exhibit different habits in the case of isolated growth versus in a group. Computational modeling based on simulations of the light-matter interactions at the growth interface was performed and successfully reproduced the experimentally observed morphologies. Analysis of light absorption in the simulated structures, as well as additional modeling of light scattering at the growth interface, provided insight into the mechanism by which the inclination effects apparent phototropic and skototropic responses. Additional depositions were performed to validate the mechanism and used inclined illumination on substrates templated with conductive islands on a series of different pitches to manipulate the optical communication between deposited features.

Se-Te was photoelectrodeposited using illumination directed along the surface normal and supplied by a linearly polarized, narrow-band light-emitting diode (LED) source that had an intensity-weighted average wavelength, λavg, of 727 nm. Figure 4.1a presents a representative scanning-electron micrograph (SEM) of the resulting deposit morphology and reveals a periodic, lamellar structure with high-aspect ratio, anisotropic features that extended out from the substrate along the normal. Figure 4.1b-h presents representative SEMs of deposits generated with the illumination inclined at an angle, α, from the surface normal and in the plane perpendicular to that of the polarization. With α = 10° (Figure 4.1b), the structure inclined with the features extending from the substrate along a vector in the same plane, but on the opposite side of the normal, as the illumination

incidence. Deposition using $\alpha = 20°$ and $30°$ (Figure 4.1c, d) resulted in structures similar to that for $\alpha = 10°$ (Figure 4.1b), but with increasing feature inclination away from the normal and from the illumination incidence. Thus, deposition with $\alpha = 10°$ to $30°$ (Figure 4.1b-d) resulted in an apparent negative phototropic, or skototropic, growth response. With $\alpha = 40°$ (Figure 4.1e) all deposit features did not consistently extend from the substrate towards one side of the normal, but instead adjacent features extended both to the same and to the opposing sides. Deposition using $\alpha = 50°$ (Figure 4.1f) resulted in structures similar to that for $\alpha = 40°$ (Figure 4.1e), but with features that primarily extended towards the same side of the normal as the illumination incidence. With $\alpha = 60°$ and $70°$ (Figure 4.1g,h) the features extended towards the same side of the normal as the incident illumination, and were more sharply inclined away from the normal than the structures observed with $\alpha = 50°$ (Figure 4.1f). Deposition with $\alpha = 60$ and $70°$ (Figure 4.1g,h) therefore effected an apparent positive phototropic growth response. These data suggest that the mesoscale morphology is broadly sensitive to the inclination of the incident illumination relative to the substrate and that this input encodes for the inclination of the deposit features in a markedly non-monotonic fashion. Additionally, for deposits generated with $\alpha = 40°$ to $70°$ (Figure 4.1e-h), the feature width and pitch were increased relative to depositions with $\alpha < 40°$. Moreover, some features with diminished heights were observed adjacent to larger, inclined features, suggesting that competitive light absorption, analogous to that observed in dense tree forest growth, may be involved in determining the deposit morphology under these conditions.[49,50]

Figure 4.1. (a)-(h) SEMs representative of photoelectrodeposits generated with λ_{avg} = 727 nm illumination incident at the indicated angle α from the substrate normal.

Photoelectrodeposition using a series of off-normal incident illumination inputs over a range of values of λ_{avg} was investigated. Figure 4.2 presents representative SEMs of deposits generated using λ_{avg} = 521, 630, 775 and 843 nm each with α = 0, 20, 40 and 60°. For all investigated cases, lamellar patterns with apparent feature sizes and pitches that scaled monotonically with λ_{avg} were observed. With α = 0° (normal incidence, Figure 4.2a-d) pattern features were observed to extend out from the substrate along the normal for each value of λ_{avg}. With α = 20° (Figure 4.2e-h) features were observed to extend from the substrate along a vector directed away from the normal and on the opposite side of the normal as the illumination incidence for each value of λ_{avg}, thus exhibiting apparent skototropic growth behavior similar to that observed for the case of λ_{avg} = 727 nm with α = 10 to 30° (Figure 4.1b-d). The magnitude of the feature deviation away from the normal appeared to scale monotonically with λ_{avg} with morphologies generated using larger values

of λ_{avg} exhibiting greater structural inclination. With $\alpha = 40°$ (Figure 4.2i-l) the features

did not consistently extend from the substrate towards one side of the normal but rather

adjacent features were observed on both the same and opposing sides. As with the case of

$\alpha = 20°$ (Figure 4.2e-h), the magnitude of the feature deviation appeared to scale

monotonically with λ_{avg} with morphologies generated using larger values of λ_{avg} exhibiting

greater feature inclination though in this case both towards and away from the same side

of the normal as the illumination incidence. With $\alpha = 60°$ (Figure 4.2m-p) features were

observed to extend along a vector directed away from the normal but on the same side as

the illumination incidence for each value of λ_{avg}, thus exhibiting apparent positive

phototropic growth behavior similar to that observed for the case of $\lambda_{avg} = 727$ nm with α

$= 60°$ and 70° (Figure 4.1g,h). This data shows that manipulation of the optical inputs to

the photoelectrodeposition can generate patterned structures displaying a range of feature

sizes, pitches and inclinations and indicates that the sensitivity of the growth to the

orientation of the illumination incidence relative to the substrate is a monotonic function

of λ_{avg}. Also, in the morphologies observed for deposits generated with $\alpha = 40$ and 60°

(Figure 4.2i-p), some lamellar features with diminished heights were observed adjacent to

larger, inclined features as observed for the case of $\lambda_{avg} = 727$ nm with $\alpha = 40$ to 70° (Figure

4.1e-h), again suggesting that competitive light absorption may be involved in the

morphology determination. The magnitude of the feature deviation away from the normal

increased monotonically with λ_{avg}, with morphologies generated using larger values of λ_{avg}

exhibiting greater structural inclination. This behavior is in contrast to that observed

previously for photoelectrodeposition on substrates templated with isolated conductive

islands to prevent optical communication between neighboring growth, in which the phototropic response was diminished with increasing wavelengths.[48] In the templated case, the phototropic response was determined to be a result of spatially asymmetric absorption that was in turn the result of attenuation of the inclined illumination input by the deposited material. This suggests, additional, ensemble optical effects are critically important in the case of unconstrainted growth on an isotropic substrate.
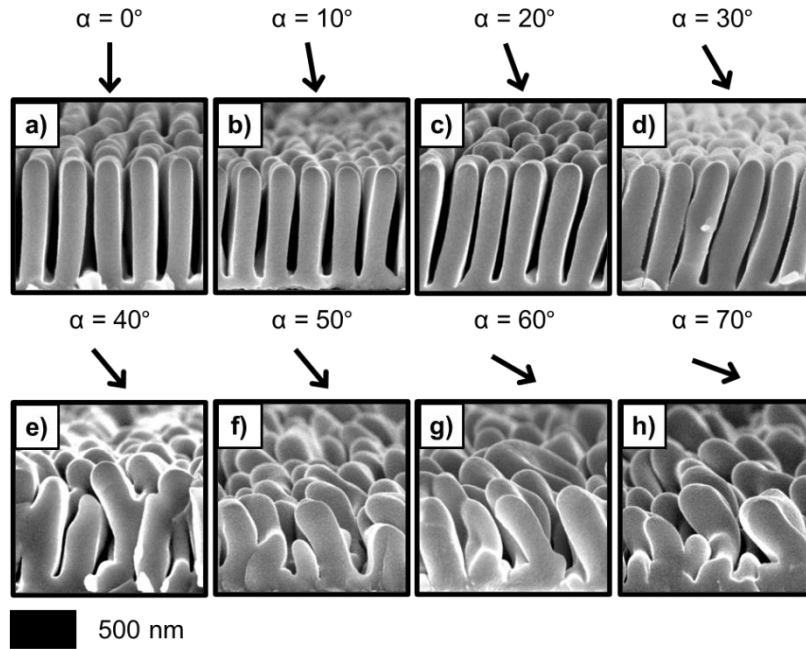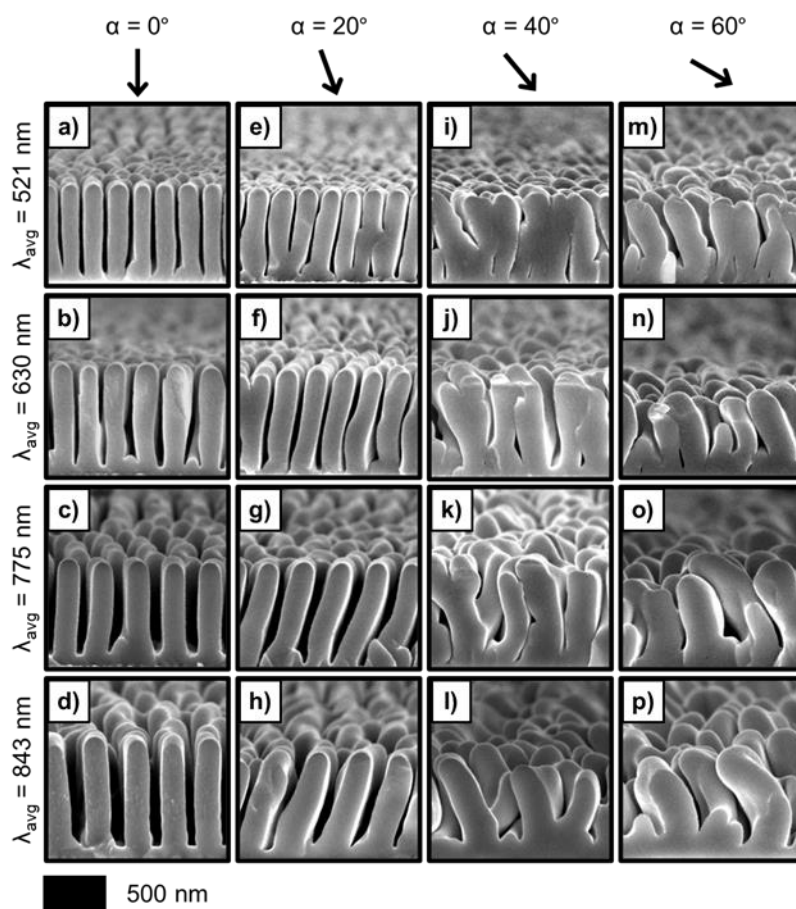
Figure 4.2. (a)-(p) SEMs representative of photoelectrodeposits generated with the indicated λ_{avg} illumination incident at the indicated angle α from the substrate normal.

Computer modeling of the growth process was performed using a two-step, iterative model in which electromagnetic simulations were first utilized to calculate the spatial profile of light absorption magnitude at the growth interface. Then, light-directed electrodeposition was simulated using a Monte Carlo method that used the local absorption to weight the local probabilities of deposition. No empirical data were used in the modeling other than estimates of the refractive index of the solution and the complex index of the Se-Te material. The computational data thus results solely from the fundamental light-matter interactions during deposition. Figure 4.3a-h presents simulated morphologies, overlaid with the light absorption profile for the associated illumination condition, for λavg = 727 nm and α = 0 to 70° in 10° increments. In each case, the simulations accurately reproduced the experimentally observed morphologies (Figure 4.1). Specifically, with α = 0° (Figure 4.3a), lamellar features were observed to extend out from the substrate along the normal, and the light absorption was localized symmetrically within features tips, consistent with normally oriented growth. With α = 30° (Figure 4.3d) apparent skototropic growth was observed in which the features extended along a vector on the opposite side of the normal as the illumination incidence, in agreement with the orientation observed experimentally under such conditions (Figure 4.1d). Notably, the light absorption was asymmetrically localized in the feature tips with greater intensity on the side away from the illumination incidence. For α = 60° (Figure 4.3g) apparent phototropic growth was observed, with most features extending along a vector on the same side of the normal as the illumination incidence, and absorption was highly localized in the tips of the lamellar features, consistent with the phototropic growth and feature orientation observed

experimentally (Figure 4.1g). The close agreement between the experimental and simulated morphologies suggests that the structures are fully determined by the characteristics of the incident illumination in conjunction with the light-matter interactions during the photoelectrodeposition. The inclined morphologies are a consequence of structural evolution to maintain effective light harvesting, as growth follows the light absorption. The simulated absorption data suggests that illumination inclination results in modulation of the near-field light intensity distribution at the growth interface in a manner that is a non-monotonic function of α. Additionally, with $\alpha = 60°$ (Figure 4.3g), some features were observed with diminished heights adjacent to larger inclined features in accord with the experimental data (Figure 4.1g), and substantial absorption localization was not observed in the shorter features, whereas the adjacent larger features exhibited intense localization, suggesting competitive light absorption effects also inpact the morphology produced under such illumination conditions. This behavior is consistent with competition in forest canopies in which trees exhibit suppressed growth and are relegated to the understory after overtopping by another tree as the environmental light availability is diminished .[51]
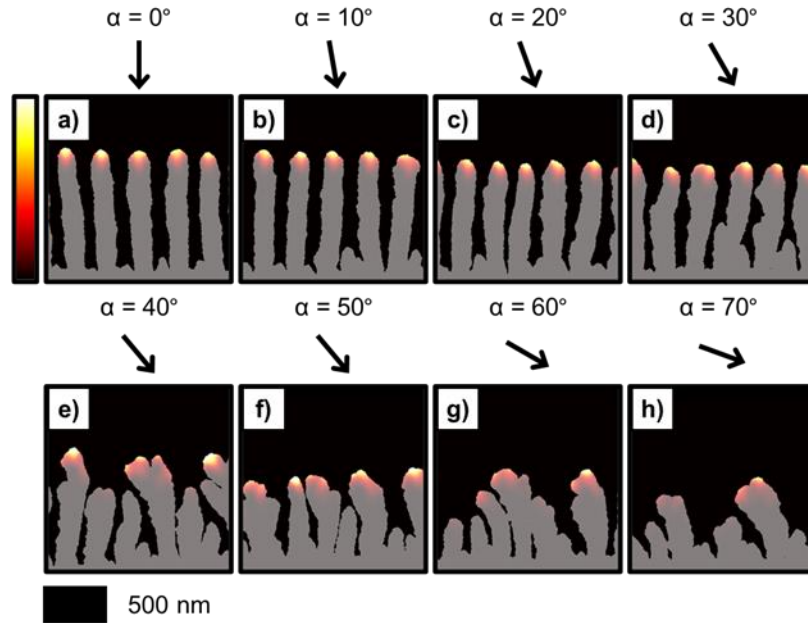
Figure 4.3. (a)-(h) Simulated photoelectrodeposit morphologies generated via growth modeling with $\lambda_{avg} = 727$ nm illumination incident at the indicated angle α from the substrate normal and overlaid with simulated absorption profiles generated with the same illumination condition.

Spontaneous order generation via inorganic phototropic growth using linearly polarized light directed at normal incidence has been shown to be a result of an emergent nanophotonic phenomenon in which lamellar features asymmetrically scatter the incident illumination towards the nearest-neighbor features, concentrating and localizing the intensity at these neighbors, and thus promoting synergistic absorption.[36] Here, additional optical simulations were performed to understand the physical mechanism by which inclination of the illumination affects the intensity distribution at the growth interface. Point dipole radiation sources were utilized to model the amplitude modulation of the electric field at the growth interface resulting from scattering of the incident illumination by the evolving lamellar features. Figure 4.4a presents a simulation of the normalized time-average electric field magnitude from two dipoles emitting radiation with a free-space wavelength of λ = 727 nm in a medium of index n = 1.33 (representative of the deposition

solution) separated by one wavelength in the direction perpendicular to the oscillation axis. This simulation is instructive for growth using illumination directed at normal incidence. Figure 4.4b presents the profile of the electric field magnitude across the horizontal centerline of the simulation presented in Figure 4.4a. An interference fringe was observed midway between the dipole sources and represents a light-intensity profile consistent with the periodic and anisotropic lamellar features produced experimentally as well as the cooperative scattering between neighboring features. Similar dipole source simulations were performed with the introduction of appropriate phase offsets between the emission of the two dipoles to account for the optical path length difference between adjacent scattering sites to effect for the case of illumination inclined at an angle α. Figure 4.4c presents intensity profiles similar to that presented in Figure 4.4b for simulations modeling the use of illumination with $\alpha = 0$, 30, and 60° with the data truncated to focus on the interference between the dipoles. The band for $\alpha = 30°$ had a positive displacement suggesting that during deposition with such illumination the nearest maximum in the interfacial scattered light intensity profile is located toward the side of the features opposite that of the far-field illumination incidence. This result is consistent with the apparent skototropic growth observed experimentally for $\alpha = 30°$ (Figure 4.1d). Strikingly, despite being oriented away from the far-field incidence direction, the growth is actually locally directed to the nearest intensity maximum. Hence, the growth is phototropic with respect to the local field, but is skototropic with respect to the direction of the far-field illumination input. The band for $\alpha = 60°$ negatively displaced relative to that for $\alpha = 0°$, suggesting that during deposition the nearest maxima in the interfacial scattered light intensity profile in

this case is directed towards the same side of the features as the far-field illumination.

This near-field phototropic growth behavior is thus fully consistent with the far-field

phototropic growth observed experimentally for α = 60° (Figure 4.1g). The contrasting

growth regimes and the non-monotonic relationship between the inclinations of the

incident far-field illumination and the deposited features, thus can be understood as a

physical consequence of the extended and periodic natures of the interfacial light intensity

profile and the deposited structure.
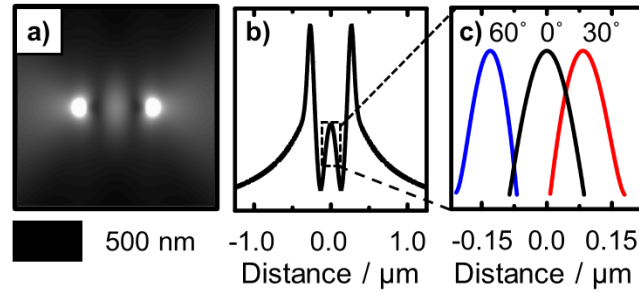
Figure 4.4. (a) Simulation of the normalized time-average electric field magnitude from two coherent dipole sources emitting radiation with a free space wavelength of λ = 727 nm in a medium of index n = 1.33 separated by one wavelength parallel to the oscillation axis. (b) Profile of the electric field magnitude across a horizontal cross-section of the simulation presented in (a). (c) Plot of the central maximum from electric field profiles similar to that presented in (b) but based on simulations with phase delays offsets between dipole emissions to model scattering of illumination inclined at the indicated angle α from the normal.

Figure 4.5 provides a schematic illustration of the notional relation between the

illumination incidence, interfacial light intensity profile and growth inferred from the light

scattering modeling using dipole sources presented in Figure 4.4. Normally-incident

illumination (Figure 4.5a) results in registry between the maxima of the spatially-

oscillating interfacial light intensity profile and the tips of the evolving lamellar features

(Figure 4.5b) and thus growth is directed along the normal (Figure 4.5c). As the

illumination incidence is inclined at a small deviation from normal (Figure 4.5d), the

intensity profile shifts relative to the deposit features in the direction of the component of the incidence vector parallel to the surface and the nearest maxima to each feature becomes slightly offset in this same direction (Figure 4.5e). Growth towards these maxima is thus apparently skototropic (Figure 4.5f). Larger inclinations of the illumination (Figure 4.5g) results in further shifting of the intensity profile relative to the deposit features and with sufficient inclination the nearest intensity maxima to each feature is localized away from the feature in the direction opposite that of the component of the incidence vector parallel to the surface (Figure 4.5h). Growth towards such maxima is thus apparently positively phototropic (Figure 4.5i). Thus, the data suggests that at the subwavelength scale solely a positively phototropic mechanism is operative independent of the inclination of the illumination input as feature growth is directed by growth towards local intensity maxima. Apparent skototropic and phototropic responses are observed with respect to the far-field incidence as the optical interactions between the illumination and the evolving structure redistributes the field intensity in the subwavelength vicinity of the growth interface.
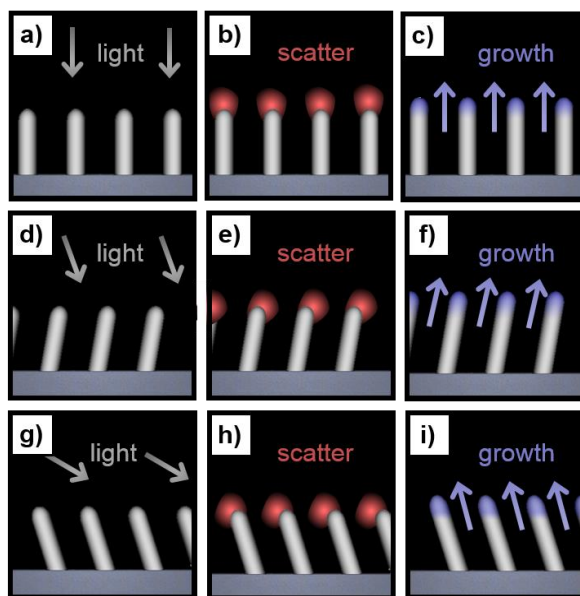
Figure 4.5. Schematic illustration of the mechanism of feature growth in response to normal and inclined illumination inputs. For normally-incident illumination (a) scattering directs and enhances the local light intensity near the tips of the features (b), and growth is directed along the normal (c). For illumination inclined slightly away from normal (d) scattering directs and enhances the local light intensity near the tips of the features but offset towards the side away from the illumination incidence (e) and growth is directed by and towards these intensity maxima, away from original illumination incidence (f), thus demonstrating apparent skototropism. For illumination incident in a manner similar to that in (d) but inclined at a greater angle away from normal (g) scattering directs and enhances the local light intensity near the tips of the features but offset towards the side of the illumination incidence (h) and growth is directed by and towards these intensity maxima, towards the original illumination incidence (i), thus demonstrating phototropism.

To further verify that growth is always positively phototropic in the near-field, and that any apparent skototropic behavior is a consequence of emergent optical phenomena, photoelectrodeposition using $\lambda_{avg} = 727$ nm illumination inclined at $\alpha = 30°$ was performed on circular Au islands on square pitches of 4.0, 0.6, and 0.4 μm, that were lithographically patterned on a n+-Si substrate. Photoelectrodeposition on the 4.0 μm pitch resulted in asymmetrical hemispherical deposits with greater mass on the side of the illumination incidence relative to the opposite side (Figure 4.6a), consistent with the far-field positive phototropic growth observed in previous examination of optically isolated deposits.[48] Photoelectrodeposition on the 0.6 μm pitch also resulted in asymmetrical hemispherical

deposits, but with greater mass on the side opposite that of the incident illumination (Figure 4.6b) and thus such growth was apparently skototropic. Growth on the 0.4 μm pitch resulted in mostly symmetrical deposits (Figure 4.6c). The observation of different morphologies, and both apparent phototropic and skototropic growth regimes, despite a single common illumination input indicates an emergent effect. Photoelectrodeposition on the templated substrates was simulated using the iterative growth model, and the associated light absorption profiles were generated and are presented in Figure 4.6d-f. The simulated morphologies agreed with the experimental data, suggesting that the emergent effect is optically based as the model considered only optical interactions. For the case of the 4.0 μm pitch, the simulated absorption profile revealed an absorption maximum near the top of the deposit on the side of the incident illumination (Figure 4.6d). For the 0.6 μm pitch, the absorption maximum was located near the top of the deposit on the side opposite that of the illumination incidence (Figure 4.6e). This is consistent with local phototropic growth despite a skototropic response in relation to the far-field illumination input. Moreover, the intensity of the absorption was greater in the 4.0 μm case than the 0.6 μm case, consistent with cooperative scattering amongst proximate features.[36] For the 0.4 μm pitch, the absorption maximum was located at the top of the deposit (Figure 4.6f), consistent with the symmetric morphology. The location of the maximum in this case was again consistent with notion that deposition is consistently locally phototropic regardless of any apparent far-field response. Additionally, the differences in the morphologies generated for different spacings was again similar to that observed for growth of certain tree species in isolation relative to that in proximate groupings.
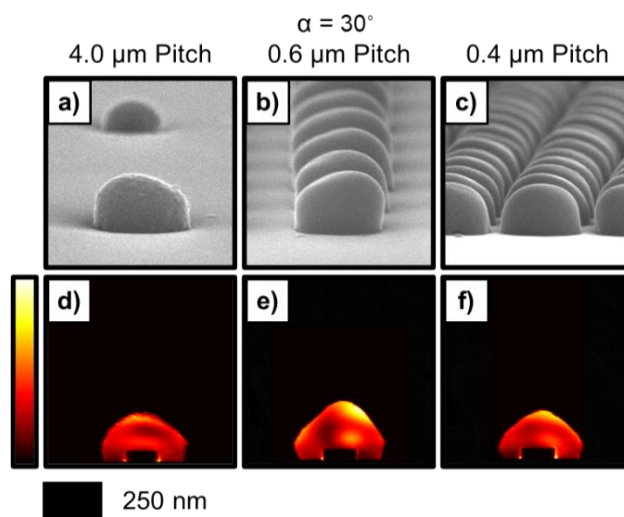
Figure 4.6. (a)-(c) SEMs representative of photoelectrodeposits generated with λ_{avg} = 727 nm illumination incident at α = 30° from the normal on substrates patterned with conductive islands on the indicated square pitch. (d)-(f) Simulated illumination absorption profiles generated via growth modeling using the same illumination conditions and pitches as in (a)-(c).

Phototropic growth provides for phenotypic plasticity in plants and enables the expression of different morphologies depending on the available illumination to maximize fitness in variable environments despite a lack of motility and a fixed genotype.[52] Gravitropic growth in response to position within a gravitational field also provides for fitness supporting morphological plasticity in plants.[53] This biological definition of plasticity, an adaptive property, is distinct from the materials definition, a mechanical property. However, the adaptive, biological concept can be descriptive of the photoelectrochemical material deposition in which new growth is projected to optimize light harvesting and thus producing a structure that is tailored to the optical environment, despite a fixed material identity. Such morphology shaping during inorganic material growth is fully phototropic and not subject to a gravitropic response, nor other control mechanisms as indicated by the success of the fully optical growth model. Comparable phototropic responses are difficult to observe in natural systems as off-normal phototropic

growth typically elicits an antagonistic gravitropic response.[54] Figure 4.7a presents an image of a Cook pine conifer (*Araucaria columnaris*) in Pasadena, CA, USA which exhibits a pronounced southern tilt. The off-normal growth habit is posited to be a result of a potentially deleterious impairment of gravitropic function in Cook pines.[55] The orientations of 256 Cook pines in 18 regions separated by > 500 km from each other and across 5 continents is presented in Figure 4.7b as a function of geographic latitude. Pines in the northern hemisphere oriented southward, pines in the southern hemisphere oriented northward, and a linear correlation between the magnitude of the orientation and the geographic latitude of the pine location was observed. Figure 4.7c presents orientation data analogous to that in in Figure 4b but for features in photoelectrodeposited Se-Te with λavg = 727 nm illumination as function of inclination (α). Figure 4.8 presents this same data as a series of histograms to clarify the distribution of orientations observed for each input inclination. For $\alpha = 0°$, $20°$, and $30°$, a narrow distribution of orientations was observed with near zero magnitudes for $\alpha = 0°$ and negative magnitudes for $\alpha = 20°$ and $30°$. For $\alpha =$ 40°, the largest distribution of orientations was observed with both positive and negative magnitudes whereas for $\alpha = 60°$, a distribution of positive orientations, including the largest magnitudes observed for all assessed values of α, were observed. The Cook pine data is consistent with phototropic growth towards time-averaged position of the sun. This mechanism is supported by the fact that morphological orientation in both the natural and photoelectrodeposition cases is understood to be spatially inclined towards the direction of greater local light intensity. Nevertheless, the lack of linearity in relation between the photoelectrochemical deposit feature orientation and α, as observed for the Cook pine

orientation and latitude, is further evidence for response modulating ensemble optical phenomena.

Tree crown shapes can exhibit substantial plasticity in response to environmental light conditions that are dictated by the presence of neighboring trees.[55,56] Oak trees grown in isolation typically develop hemispherical crowns whereas oak trees grown in dense forest stands establish foliage only at the top of the trunk.[49] Artificial gaps generated in Douglas fir forests that were previously thinned to a consistent spacing resulted in asymmetric growth of the trees adjacent to the gaps and the crown size of the border trees significantly exceeded that of the interior trees.[57] Similarly, the interfacial feature width, as well as the pitch, of the structures generated via inorganic phototropic growth were a function of the input illumination condition and for a given λ_{avg} appeared to scale with α (Figure 4.7d). The interfacial feature pitch of deposits generated using $\lambda_{avg} = 727$ nm illumination was measured via two-dimensional Fourier transform analysis of SEM data and is presented in Figure 4d as a function of α. The interfacial feature width of the $\lambda_{avg} = 727$ nm deposits was measured directly from the SEM data and is presented in Figure 4.7e on a relative scale as a function relative feature pitch. Figure 4.7e also presents the crown width as a function of tree pitch on the same relative scale for mature white spruce, black spruce, and red pine trees.[58] The tree stand data is derived from a spacing trial in which each tree species was planted at three fixed distances on a square pitch and no thinning or pruning was performed. The relationships between the relative width and pitch were linear and mutually similar for the photoelectrodeposited structures and each of the tree species. The similarity between the growth characteristics of the natural and inorganic systems

suggests that adaptive photomorphogenesis that maximizes light collection in ensemble systems produces general scaling relations that are independent of the underlying microscopic processes. This is consistent with the results from modeling investigations, including game-theory, individual-based, and propagating-front approaches, that examined emergent, light-directed habit formation in tree stands.[49,51,59] Figure 4.7f presents the same growth characteristic data of the photoelectrodeposited structures as Figure 4.7e but with the abscissa rescaled to represent relative linear feature density. Figure 4.7f also presents the crown width of stand grown Douglas fir trees as a function of relative linear tree density which was described by a linear relationship similar to that of the inorganic system. The Douglas fir data was obtained from measurements of naturally developed stands in which the relative tree positions and densities were not artificially predetermined by planting. Such development is thus analogous to the spontaneous structure determination in template-free inorganic phototropic growth. The similarity in the growth of the fully self-organized natural and inorganic systems further supports that light-mediated emergent growth dictates general scaling relations.
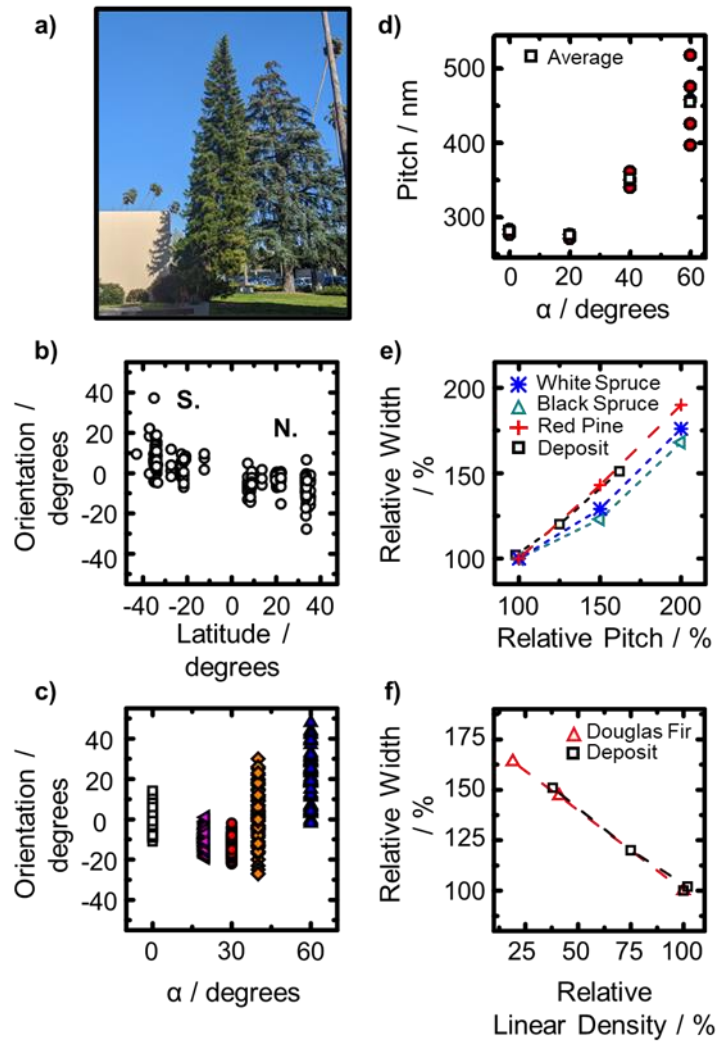
Figure 4.7. (a) Image of Cook pine exhibiting an off-normal growth habitat. (b) Orientation of 256 Cook pines as a function of latitude (adapted from reference 55). (c) Orientation and (d) pitch of features in photoelectrodeposits generated as a function of the incident illumination inclination from the normal, α. Relative crown width of photoelectrodeposit features as well as (e) planted trees, and (f) forest grown trees, as a function of relative pitch, and relative change in linear density, respectively (tree data adapted from references 61 and 62). All photoelectrodeposits generated using λ_{avg} = 727 nm illumination.
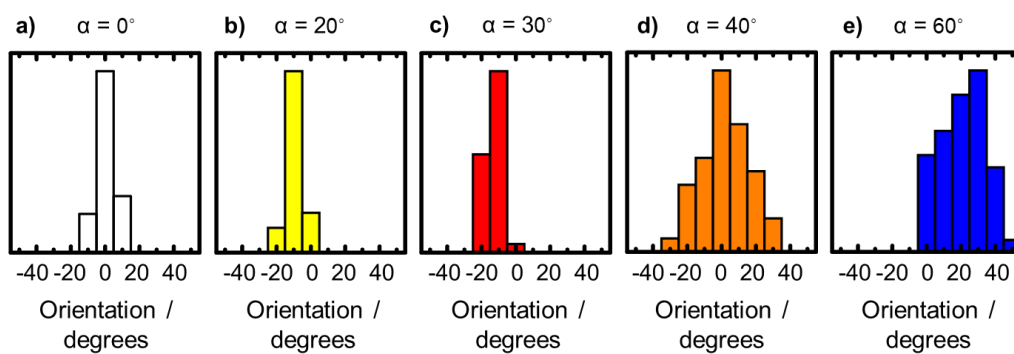
Figure 4.8. (a)-(d) Orientation histograms of the photoelectrodeposite features with $\lambda_{avg} = 727$ nm illumination incident at the indicated angle α from the substrate normal.

4.3 Conclusions

The collective data indicates that template-free photoelectrodeposition of an inorganic semiconductor on an isotropic substrate using inclined illumination can generate mesostructured deposits with inclined nanoscale features that orient in a phototropic manner. The feature orientation is a non-monotonic function of the inclination of the input and both phototropic and skototropic regimes with respect to the far-field incidence direction were observed. However, the response was consistently phototropic with respect to the subwavelength scale optical intensity profile at the growth interface. Emergent interfacial light scattering directed inclined feature growth and generated the apparent skototropic response. Comparison of the photoelectrodeposit morphologies to the growth habits of a series of tree species shaped by light availability revealed striking similarities in the geometries despite the disparate length scales. This suggests potential commonalities in the light harvesting behavior in both inorganic and biological systems. Additionally, the responsive process may be expanded upon to yield a new biomimetic paradigm for the construction of mesoscale architectures based on anisotropic and dynamic material growth to tailored illumination.

Chapter 5

INCLINATION OF POLARIZED ILLUMINATION INCREASES SYMMETRY OF STRUCTURES GENERATED VIA INORGANIC POHOTOTROPISM

Meier, M.C.; Lewis, N. S.; Carim, A. I. Inclination of Polarized Illumination Increases Symmetry of Structures Grown via Inorganic Phototropism. *In Preparation.*

5.1 Introduction

We demonstrate that Se-Te photoelectrodeposits fabricated using inclined illumination along the plane of incident polarization results in defect reduction and overall improved fidelity in nanostructured thin films. Optically-based growth modeling with inclined illumination displayed similar enhancements in film order indicating that this change in feature morphology was an optically-based mechanism. Further modeling indicated decoupling from off-axis scattering sites at angled illumination lead, to feature formation directed solely by on-resonant and axis features ultimately resulting in improved film order.

5.2 Results and Discussion

Figure 5.1a presents a scanning-electron micrograph (SEM) of a deposit generated via inorganic phototropic growth using vertically polarized $\lambda_{avg} = 626$ nm illumination at normal incidence. The SEM reveals a periodic lamellar morphology with a net orientation of the lamellar long axes towards the vertical. Along the length, individual lamellar features were sinuous and exhibited alternating deviations from vertical alignment as well as fluctuations in width. Dislocation defects in which two adjacent features exhibited segments that were oriented off-axis and converged to a single feature were also observed. Figure 1b and c present SEMs of deposits generated using the same illumination as in Figure 1a, but inclined from the substrate normal in the plane of the polarization by an angle, β, of 20° and 40°, respectively. For $\beta = 20°$ the alignment of individual features exhibited a lower frequency of deviations from the vertical than for normal incidence ($\beta = 0°$, Figure 5.1a) but off-axis feature segments and dislocation defects were still observed. The feature width was also more consistent along the length. For $\beta = 40°$, off-axis feature alignment was substantially reduced relative to the $\beta = 0°$ and 20° cases and the structure translational symmetry in both the vertical and horizontal directions was enhanced. Thus, inclination in the plane of the polarization of the illumination input to the inorganic phototropic growth process appeared to improve the fidelity of the resultant mesostructures.

β = 0°   β = 20°   β = 40°
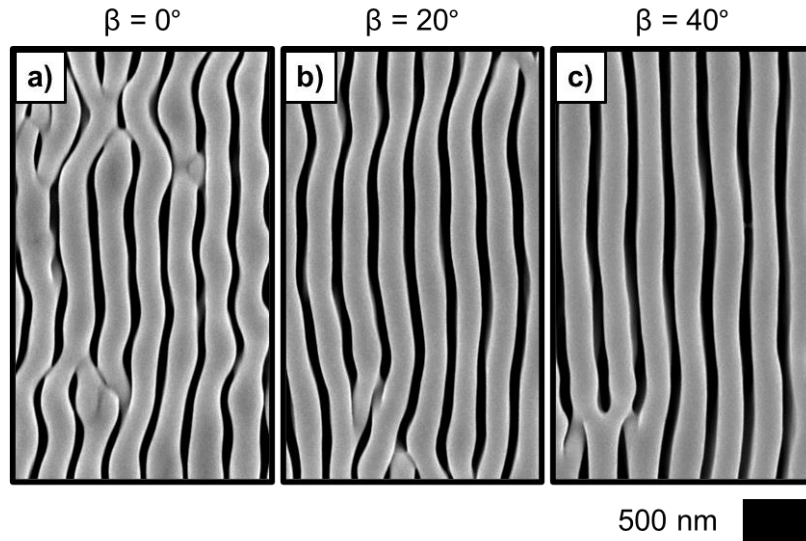
Figure 5.1. (a)-(c) Representative SEMs for λ_{avg} = 626 nm at the indicated angle β.

Fourier analysis was utilized to assess the order of the deposits generated via inorganic phototropic growth using both normally incident and inclined illumination. Figure 5.2a-c present two-dimensional Fourier transforms (2D FT) generated from SEMs of a deposit produced using β = 0°, 20° and 40°, respectively. Intensity in each FT is indicative of a spatially periodic morphology component in the deposit from which the FT was derived. The displacement distance from the center of the FT is the spatial frequency and the direction of the displacement is the direction of the spatial periodicity. For all three values of β, the 2D FTs were characterized by a single set of intense bands aligned along the horizontal, consistent with the anisotropy and horizontal periodicity in the deposit morphologies (Figure 5.1). Figure 5.2d presents Fourier spectra representing the intensity profiles along the horizontal centerlines of the 2D FTs for β = 0° and 40° (Figure 5.2a and c). The spectra were qualitatively similar and revealed a single family of harmonics, indicative of the generation of a morphologies with a single narrow range of pitch values.[1]

The sizable overtone intensity is consistent with the sharp contrast in the SEM data (Figure 5.1) and thus the significant structural anisotropy. The structure topologies cannot be fully represented by single sinusoidal function and are more fully described by a function more like a square-wave which requires the higher-frequency overtone intensity to approximate. The harmonic bandwidths for $\beta = 40°$ were qualitatively narrower than for $\beta = 0°$, indicating a more consistent feature pitch across the interface. The Fourier spectra for $\beta = 40°$ also showed less intensity at zero frequency as well as lower baseline intensity relative to $\beta = 0°$, indicating a lesser amount of aperiodic morphological components and more well-defined order.

Notably, the intensity bands in the 2D FT associated with the $\beta = 0°$ SEM data (Figure 5.2a) had finite height in the vertical direction (perpendicular to the direction of the morphological periodicity) with the band height increasing with each successive harmonic. Such intensity off the horizontal axis is consistent with the observed off-axis feature alignments (Figure 5.1a). The vertical height of the bands as well as the degree of height increase in the successive overtones was reduced for $\beta = 20°$ (Figure 5.2b) and further diminished for $\beta = 40°$ (Figure 5.2c), consistent with the improved feature alignment generated with the inclined illumination inputs. Figure 5.2e presents a Fourier spectrum representing the intensity profile across the vertical centerline of the positive fundamental mode of the 2D FT for $\beta = 40°$ and associated fit curve (the positive and negative modes are degenerate due to the intrinsic symmetry of the 2D FT so the choice of mode for analysis is arbitrary). Figure 5.2f presents the full width at half maximum (FWHM) of similar fit curves for both the fundamental and first overtone modes of each 2D FT as a

function of β. The FWHM of both modes for β = 40° was approximately 60 % lower relative the that for β = 0° and intermediate values were observed for β = 20°. This analysis confirmed the apparent fidelity improvement effected by the use of inclined illumination was largely the result of a reduction of off-axis morphological order. The large absolute decline in the overtone FWHM with increasing β, a decline more than twofold of that in the fundamental FWHM, is indicative of substantially diminished off-axis topological contrast.
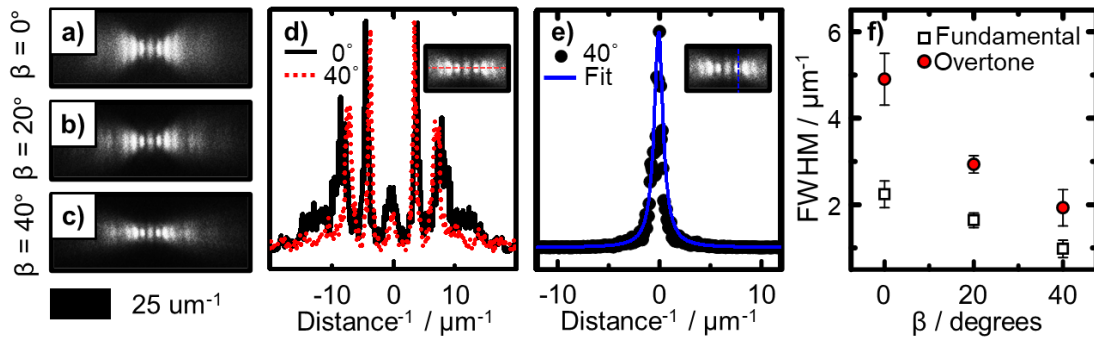
Figure 5.2. (a)-(c) 2D Fourier transforms for λ = 626 nm at the indicated angle β. (d) Profile of the center horizontal lines for the 2D FTs presented in (a) and (c). (e) Profile of the vertical centerline of the fundamental mode of the 2D FT for β = 40° and fit. (f) Full width at half maximum (FWHM) of fit curves for fundamental and first overtone modes of (a)-(c).

A series of simulations were performed to elucidate the mechanism by which inclination of the illumination input to inorganic phototropic growth improves alignment and reduces off-axis order in the resultant structures. Growth was simulated using an optically-based, two-step iterative model.[28,30] First, an electromagnetic simulation was used to calculate the local light absorption profile. Next, a Monte Carlo simulation was performed to simulate growth in which the absorption profile profile was used to define the probability of local material addition, and then the process was iterated. Empirical

inputs to the model were limited to estimates of the deposition solution index and the deposit complex refractive index. Figure 5.3a-c presents simulated morphologies generated via growth modeling using vertically polarized $\lambda_{avg} = 626$ nm illumination inclined at $\beta = 0°$, 20° and 40°, respectively. In all cases, the simulated morphologies qualitatively reproduced the experimental results (Figure 5.1). For $\beta = 0°$, the lamellar features were sinuous and exhibited variable width along length, and also dislocation defects were observed (Figure 5.3a). For $\beta = 20°$, the alignment variance of local features segments was decreased, and the feature width along a single lamellar feature more consistent, than with $\beta = 0°$. For $\beta = 40°$, greater linearity was observed along the length of the individual features than for $\beta = 0°$ and 20°. The agreement between the results of the model, generated by considering only optical interactions, and the experimental data indicated a photonic basis for the fidelity improvement observed for the use of inclined illumination.
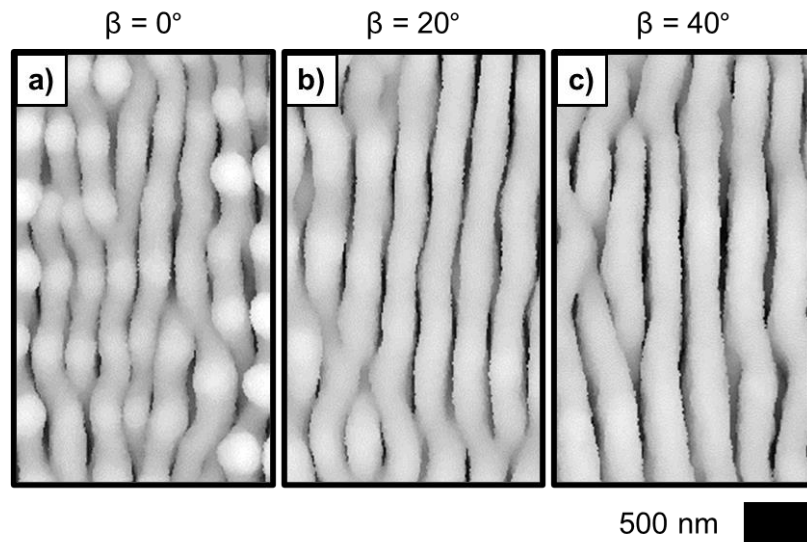
Figure 5.3. (a)-(c) Simulated growth model structures for $\lambda_{avg} = 626$ nm at the indicated angle β.

Structure generation via inorganic phototropic growth is a product of inherent asymmetries in the interfacial light-matter interactions that shape the local optical field profile which in turn directs the local rates of photoelectrochemical deposition. Electrochemical growth on an isotropic substrate generates surface texture which can scatter the incident illumination. The linear polarization results in directional scattering and interference between scattering sites results in spatially-varying filed intensity that drives spatially-varying mass addition rates across the substrate. The amplitude modulation of the electric field at the growth interface resulting from scattering of the incident illumination was modeled for $\beta = 0°$ and $40°$ using point dipole radiation sources. Figure 4a,b depict the time averaged electric field for $\lambda_{avg} = 626$ nm separated by one wavelength at $\beta = 0°$ and $40°$ for Figure 4a and Figure 4b, respectively. In both cases a center band was observed, consistent with the periodic, anisotropic features observed in the photoelectrochemical deposits. Figure 4c presents profiles of the vertical centerlines of the electric field in Figure 4a and Figure 4b. The intensity in the interference fringe for $\beta = 40°$ was overall higher in magnitude across the profile than that of $\beta = 0°$ suggesting in the case of inclined illumination a greater intensity in phototropic force directs lamellar feature formation consistent with the improvement in observed feature order. In the photoelectrochemical growth process the initial surface roughness and sites that scatter incident illumination are randomly distributed. If the scattering sites are pre-seeded to be in resonance with the expected feature periodicity, the observed morphology of the resulting film has improved fidelity and order due to optimized nearest neighbor interference.[36,60] Figure 4d presents the time average electric field for $\lambda_{avg} =$ 626 nm for $\beta = 0°$ separated by one wavelength but with an offset in the vertical direction to

mimic the random distribution of scattering sites initially present on the substrate surface.

An interference fringe similar to that of Figure 4a is observed but with intensity in the off-axis orientation. Figure 4e presents a similar simulation to that in Figure 4d but for $\beta = 40°$ with the appropriate phase offset. In contrast to Figure 4d for $\beta = 40°$ (Figure 4e) no intensity in the off-axis orientation is observed. Figure 4f presents profiles along the off-axis orientation of the scattering sites for the electric field in Figure 4d and Figure 4e. The off-axis band intensity for $\beta = 40°$ is substantially lower than that of $\beta = 0°$ suggesting that for inclined in-plane illumination decoupling of off-resonant scattering sites may result improved feature fidelity and observed order as primarily on axis scattering sites contribute to lamellar feature formation.
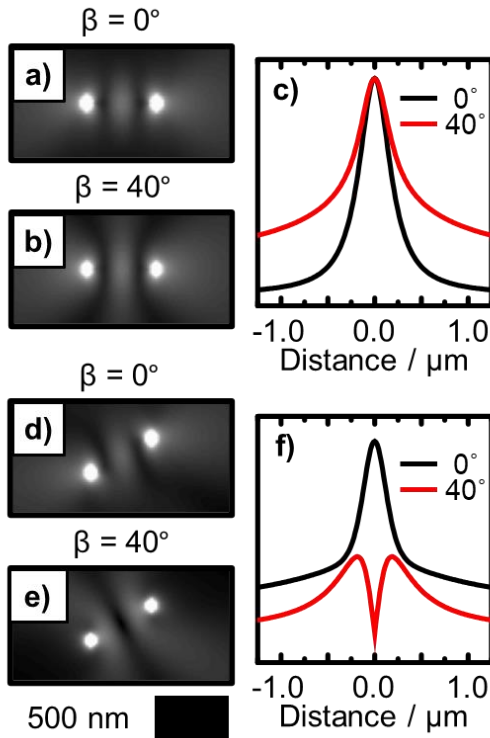
Figure 5.4. (a) and (b) Simulated time-average of electric field magnitude from two for $\lambda_{avg} = 626$ nm in a medium of index n = 1.33 for at the indicated β. (c) Profile of the center vertical lines for the simulations presented in (a) and (b). (d) and (e) Simulated time-average of electric field magnitude from two dipoles

offset along the vertical direction for $\lambda_{avg} = 626$ nm in a medium of index n = 1.33 for at the indicated β. (f) Profile of the center off-axis lines for the simulations presented in (d) and (e).

5.3 Conclusions

In summary, improved feature order and fidelity in photoelectrodeposited features produced via inorganic phototropic growth was demonstrated using inclined illumination. Simulated growth morphologies agreed with the changes in feature order, indicating that the morphologies are primarily directed by an optical mechanism. Simulations of the time-averaged field intensity for on and off-axis scattering sites revealed that the morphological response results from enhanced field intensity of on-axis scatterers and decoupling from off-axis sites.

Chapter 6

METHODS

This chapter details the experimental and computational methods used to generate the data presented in the preceding chapters.

6.1 Materials and Chemicals

H_2SO_4 (ACS Reagent, J. T. Baker), buffered HF improved etchant (Transene), In (99.999 %, Alfa Aesar), Ga (99.999 %, Alfa Aesar), SeO_2 (99.4 %, Alfa Aesar), and TeO_2 (99+ %, Sigma-Aldrich) were used as received. H_2O with a resistivity $\geq$ 18.2 MΩ cm (Barnstead Nanopure System) was used throughout. Au-coated n^+-Si(100) (< 0.005 Ω cm, As-doped, 525 ± 25 µm thick, single-side polished, Addison Engineering) was coated with Au and used as a substrate for deposition as noted in the subheadings below (*Isotropic Substrate Preparation* and *Patterned Substrate Preparation*). Flash-Dry Ag Paint (SPI Supplies), EP21ARHTND Epoxy (MasterBond), and nitrocellulose-based nail polish were used to assemble the working electrodes.

6.2 Substrate Preparation

For isotropic substrates, n^+-Si wafers were etched with buffered HF for 30 s, rinsed with H_2O, dried under a stream of $N_2(g)$, and then immediately transferred to an electron-beam metal evaporator with a base pressure $< 10^{-5}$ torr. Using an accelerating voltage of 10 kV, a 10 nm Ti adhesion layer was deposited on the polished side of the wafer using a 50 mA deposition current and then a 50 nm Pt capping layer was then deposited atop using a 150 mA current. The wafers were then transferred to a RF sputterer and 100 nm of Au was deposited on top of the Pt using a RF power of 80 W. The Au-topped Si sections were then cut into square 0.50 cm by 0.50 cm sections for use as deposition substrates.

For patterned substrates in Chapters 2 and 4, n^+-Si wafers were rinsed with acetone and isopropanol. Bi-layer resist for electron-beam lithography composed of poly(methyl methacrylate) (PMMA) was then applied by spin-coating. First, a base layer of 495 PMMA A4 was at 4000 rpm for 1.0 min and then baked at 180 °C for 3.00 min. Second, an overlayer 950 PMMA A4 was applied at 4000 rpm for 1.0 min and then baked at 180 °C for 3.0 min. Next, a VISTEC EBPG 5000+ electron-beam pattern generator was used to pattern 150 nm diameter circles with 0.4 μm, 0.6 μm, 4.0 μm, and 8.0 μm pitches in a square lattice in the resist. Pattern generation was effected using a 100 kV accelerating voltage, 300 μm aperture, 5 nA current, and a dose of 1000 μC cm^{-2}. After electron-beam pattern generation, the substrates were immersed in mixture of methyl isobutyl ketone:isopropanol in 1:3 volume ratio for 1.0 min at room temperature to develop the pattern and effect hole arrays. Next, the substrates were etched with buffered HF for 0.5 min, rinsed with H_2O, dried under a stream of $N_2(g)$, and then immediately transferred to

an CHA Mark 40 electron-beam metal evaporator with a base pressure of 10^{-6} torr. A 5 nm thick Ti adhesion layer was first deposited at a rate of 0.5 nm s^{-1} and then a 50 nm thick Au layer was deposited atop at a rate of 0.1 nm s^{-1}. The substrates were then removed from the evaporator and immersed in acetone to remove the remaining resist to effect a Si substrate patterned with Ti/Au circles. The patterned substrates were then cut into square 0.50 cm by 0.50 cm pieces using a Dynatex GST-150 scriber-breaker system for use as a deposition substrates.

For patterned substrates in Chapter 3, n + -Si wafers were first rinsed with acetone and isopropanol. PMMA resist was then applied by spin-coating for 1.0 min to effect a 0.8 µm thick layer and then cured for 5.0 min at 180 °C. Patterns consisting of circles with diameters of 0.2, 0.4, 0.8, 1.2, and 1.6 µm, on a square lattice with a pitch of 10 µm, were designed using AutoCAD (Autodesk) and fractured using BEAMER (GenISys). A Raith EBPG 5000+ electron-beam pattern generator was used to write the patterns into the resist with a 100 kV accelerating voltage, 300 µm aperture, 5 nA current, and a dose of 1000 µC cm^{-2}. The pattern was then developed by immersing the substrates in a mixture of methyl isobutyl ketone : isopropanol in a 1 : 3 volume ratio for 1.0 min at room temperature, producing an array of circular well structures. The patterned wafers, along with additional unpatterned Si, were then cut into square 0.40 cm by 0.40 cm sections using a Dynatex GST-150 scriber-breaker system; these square pieces were then used as substrates for the photoelectrochemical growth of Se-Te.

6.3 Electrode Preparation

Electrode assemblies were prepared by applying epoxy to two Al half-round bars (0.25 in diameter) on the flat sides and the two bars were then joined together with a ca. 0.4 in offset in the axial dimension to form a cylinder with two half-round ends. Polytetrafluoroethylene heat-shrink tubing was applied to insulate the cylindrical section and epoxy was used to insulate the rounded side of one of the half-round ends. A eutectic mixture of Ga and In was scratched into the unpolished back surfaces of the Au-topped Si sections with a carbide-tipped scribe. Ag paint was then applied atop the eutectic and the Au-topped Si section was affixed to the flat surface of the epoxied half-round end. Nail polish was applied to insulate the remaining uncovered area on the flat surface surrounding the Au-topped Si section. Immediately before deposition, the surface of each electrode was briefly cleaned using a stream of $N_2(g)$.

6.4 Electrode Illumination

Illumination for the photoelectrodepositions was provided by narrowband light-emitting diode (LED) source (Thorlabs) with intensity-weighted average wavelength, λ_{avg}, values and spectral bandwidths (FWHM) of 521 nm and 31 nm (M530L2), of 528 nm and 32 nm (SOLIS-525C), 630 nm and 18 nm (M625L3), 727 nm and 37 nm (M730L4), 775 nm and 30 nm (M780LP1), 843 nm and 30 nm (M850L3), and 934 nm an 55 nm, respectively.

In general, the output of the diode source was collected and collimated with an aspheric condenser lens (Ø50.8 mm, f = 32 mm). For Chapter 3, The output of the diode source was collected, condensed, and collimated using a series of three lenses: an aspheric lens (Ø25.4 mm, f = 16 mm), followed by a bi-convex lens (Ø50.8 mm, f = 16 mm), and last a plano-convex lens (Ø50.8 mm, f = 100 mm). For deposition on isotropic substrates, a dichroic film polarizer (Thorlabs LPVISE200-A or LPNIRE200-B) was placed immediately after the condenser lens to effect linear polarization. For patterned substrates, no polarizer was used. A 1500 grit ground-glass (N-BK7) diffuser was placed immediately in front of the photoelectrochemical cell to ensure spatial homogeneity of the illumination. The light intensity incident on the electrode was measured by placing a calibrated Si photodiode (Thorlabs FDS100), instead of an electrode assembly, in the photoelectrochemical cell with electrolyte, and the steady-state current response of that Si photodiode was measured.

For Chapter 2, depositions utilized illumination at normal incidence and the diode with $\lambda_{avg} = 528$ nm were performed with a light intensity of 20 mW cm^{-2}. Depositions under

illumination at normal incidence utilizing the diodes with $\lambda_{avg} = 727$ nm and 843 nm were performed with a light intensities of 40 mW cm^{-2} , and 50 mW cm^{-2} , respectively. To compensate for the decrease in the optical extinction coefficient of the Se-Te alloy with increasing wavelength from the visible to the near-infrared regime, photoelectrochemical growth with near-infrared illumination inputs was performed with greater optical intensities than were utilized for the visible illumination input. The higher illumination intensities utilized in conjunction with $\lambda_{avg} = 727$ nm or $\lambda_{avg} = 843$ nm relative to $\lambda_{avg} = 528$ nm were selected to effect the same rate of photoelectrochemical growth for each wavelength input. For depositions using illumination incident on the electrode at an angle α away from the surface normal, the intensities were increased by a factor of cos-1 (α) relative to the intensities used at normal incidence.

For Chapter 3, depositions were performed with a light intensity of 195 mW cm^{-2}. For Chapter 4, depositions utilizing illumination at normal incidence and the diodes with $\lambda_{avg} = 521$ nm and 626 nm were performed with light intensities of 20 mW cm^{-2} and 25 mW cm^{-2}, respectively. Depositions utilizing illumination at normal incidence utilizing the diodes with $\lambda_{avg} = 727$ nm, 775 nm, and 843 nm were performed with a light intensity of 40 mW cm^{-2}, 40 mW cm^{-2}, and 50 mW cm^{-2} ,respectively. For depositions using illumination incident on the electrode at an angle α away from the surface normal, intensities were increased by a factor of cos^{-1}(α) relative to the magnitudes utilized at normal incidence.

6.5 Photoelectrochemical Depostion

Photoelectrodeposition was performed using a Bio-Logic SP-200 potentiostat. Deposition was performed in a single-compartment glass cell with a pyrex window. A three-electrode configuration was utilized with a graphite-rod counter electrode (99.999 %, Sigma-Aldrich) and a Ag/AgCl reference electrode (3 M KCl, Bioanalytical Systems). Deposits were generated from an aqueous solution of 0.0200 M SeO_2, 0.0100 M TeO_2, and 2.00 M H_2SO_4. Photoelectrodeposition on isotropic substrates was effected by biasing the Au-coated electrode, illuminated as detailed under the previous subheading (*Electrode Illumination*), potentiostatically at -0.15 V vs. Ag/AgCl for 4.00 min at room temperature. For patterned substrates, deposition was effected using a two-step potentiostatic program in which deposition was first initiated using a nucleation step at a bias of -0.35 V vs. Ag/AgCl for 1.0 s and then continued at -0.15 V vs. Ag/AgCl for 0.25 min for the 0.4 μm and 0.6 μm pitches and 1.50 min for the 4.0 μm pitch, resulting in feature width of ca. 400 nm in all cases. After deposition, the electrode was immediately removed from the cell, rinsed with H_2O, and then dried under a stream of $N_2(g)$. The substrate with top-facing Se-Te photoelectrodeposit was mechanically separated from the rest of the electrode assembly. The nitrocellulose-based insulation and the majority of the Ag paint and In-Ga eutectic were then removed mechanically.

6.6 Scanning Electron Microscopy

Scanning electron micrographs (SEMs) were obtained with a FEI Nova NanoSEM 450 with a working distance of 5 mm and an in-lens secondary electron detector. Accelerating voltages of 5.00 and 15.00 kV were utilized to acquire micrographs of photoelectrodeposits on isotropic and patterned substrates, respectively. Display micrographs were acquired with a resolution of 344 pixels μm^{-1} over ca. 2 μm^2 areas. Micrographs for quantitative analysis of feature pitch and orientation were acquired with a resolution of 172 pixels μm^{-1} over ca. 120 μm^2 areas.

6.7 Raman Spectroscopy

Raman spectra were collected with a Renishaw inVia Raman microprobe equipped with a Leica DM 2500 M microscope, a Leica N Plan 50x objective (numerical aperture = 0.75), an 1800 lines mm-1 grating, and a CCD detector configured in a 180° backscatter geometry. A 532 nm diode-pumped solid-state (DPSS) laser (Renishaw RL532C50) was used as the excitation source and a 10 µW radiant flux was incident on the surface of the sample. A $\lambda/4$ plate was used to circularly polarize the incident excitation. No polarizing collection optic was used.

6.8 Energy Dispersive X-ray Spectroscopy

Energy dispersive X-ray (EDX) spectroscopy was performed in the SEM using an accelerating voltage of 15.00 kV and a working distance of 5 mm. An Oxford Instruments X-Max silicon drift detector was utilized. Spectra were collected in the range of 0 to 10 keV and quantitative deposit compositions were derived from these spectra using the "INCA" software package (Oxford Instruments).

6.9 Feature Pitch Quantification

Two-dimensional Fourier transforms (2D FTs) were generated from the SEM data. The intensity along a 15-pixel tall band across the horizontal centerline of each 2D FT was integrated resulting in a Fourier spectrum containing a family of harmonics. The fundamental mode was fit using a Lorentzian function to determine the maximum which represented the feature frequency and the reciprocal of this value was taken to yield the feature pitch.

6.10 Feature Orientation Quantification

Automated computer image analysis of cross-sectional SEM data was used to fit an elliptical shape to each figure. The orientation of the major axis of the ellipse was recorded. Histograms were generated by binning the measured values into 10˚ wide groups with centers ranging from -60˚ to 60˚.

6.11 Simulation of Film Morphology

Photoelectrodeposition was simulated with an iterative growth model wherein electromagnetic simulations were first used to calculate the local light absorption profile at the growth interface. Then, mass addition was simulated via a Monte Carlo method wherein the local absorption weighted the local rate of mass addition along the film surface. In the first step, the light-absorption profile was calculated using full-wave finite-difference time-domain (FDTD) simulations with periodic boundary conditions along the substrate interface. In the second step, a Monte Carlo simulation was performed in which fixed amount of mass was added to the upper surface of the structure with a probability F:

$$F(A) = A \prod_{i=1}^{n} \frac{x_i}{r_i} \text{ (\textbf{Equation 1})}$$

where A is the spatially dependent photocarrier-absorption at the deposit/solution interface, n is the dimensionality of the simulation (2 or 3), x_i is the fraction of ith nearest neighbors occupied in the lattice, and r_i is the distance to the ith nearest neighbor. The multiplicative sum in the definition of this probability (Equation 1) serves to reduce the surface roughness of the film so as to mimic the experimentally observed surface roughness. After the initial Monte Carlo simulation, the absorbance of the new, structured film was then calculated in the same manner as for the initial planar film, and an additional Monte Carlo simulation of mass addition was performed. The computational process was further iterated until the simulated morphologies achieved heights equivalent to those observed experimentally. Previously measured values of the complex index of refraction for Se-Te were utilized.[28] A value of n = 1.33 was used as the refractive index of the electrolyte, regardless of wavelength.[61] The simulated sources provided illumination with

maximal intensity $\lambda = 727$ nm. All FDTD simulations were performed using the "FDTD Solutions" software package (Lumerical).

For modeling of growth on isotropic substrates, two-dimensional simulations were utilized ($n = 2$) and discretized using a square mesh with a lattice constant of 2 nm. The simulations began with a bare, semi-infinite planar substrate. A linearly polarized, plane-wave illumination source was simulated. For simulations using normally-incident illumination, periodic boundary conditions were utilized in the direction parallel to the substrate plane whereas for simulations with inclined illumination Bloch boundary conditions were used. Perfectly matched layer boundary conditions were utilized in the orthogonal direction in both cases. The amount of mass added in each Monte Carlo simulation equaled that of a 15 nm planar layer.

For modeling growth on patterned substrates, three-dimensional simulations were utilized ($n = 3$) and discretized using a cubic mesh with a lattice constant of 5 nm. The amount of mass added in each Monte Carlo simulation equaled that of a 1 nm planar layer over the area of the templated conductive island. Two fully out-of-phase plane-wave illumination sources with the same incident direction (inclined 30° from the substrate normal) and orthogonal linear polarizations were simulated simultaneously. Perfectly matched layer boundary conditions were utilized in the direction normal to the substrate. Periodic and Bloch boundary conditions were utilized in the in-plane directions orthogonal and parallel to the plane of illumination inclination, respectively.

6.12 Dipole Simulations

FDTD simulations of dipole emission were used to model the effect of illumination inclination on the optical field profile generated by light scattering at the growth interface. A two-dimensional simulation plane discretized using a square mesh with a lattice constant of 1 nm and a background index of 1.33 were utilized. Dipole emission with a free space wavelength of $\lambda = 727$ nm was simulated. The dipoles were separated by one wavelength in the medium and the oscillation axis was set perpendicular to the separation axis. A phase angle between the emission from each dipole was introduced to model the delay between stimulation of adjacent scattering sites. Perfectly matched boundary conditions were utilized in both directions.

Bibliography

(1) Liu, Y.; Wu, M.; Zhang, Z.; Lu, J.; Xu, K.; Zhu, H.; Wu, Y.; Wang, B.; Lei, W. A Review on Applications of Functional Superhydrophobic Surfaces Prepared by Laser Biomimetic Manufacturing. *J. Mater. Sci.* **2023**. https://doi.org/10.1007/s10853-023-08217-9.

(2) Liao, Y.; Chen, J.; Zhang, D.; Wang, X.; Yuan, B.; Deng, P.; Li, F.; Zhang, H. Lotus Leaf as Solar Water Evaporation Devices. *Mater. Lett.* **2019**, *240*, 92–95. https://doi.org/10.1016/j.matlet.2018.12.133.

(3) Liu, K.; Du, J.; Wu, J.; Jiang, L. Superhydrophobic Gecko Feet with High Adhesive Forces towards Water and Their Bio-Inspired Materials. *Nanoscale* **2012**, *4* (3), 768–772. https://doi.org/10.1039/C1NR11369K.

(4) Cho, N. H.; Guerrero-Martínez, A.; Ma, J.; Bals, S.; Kotov, N. A.; Liz-Marzán, L. M.; Nam, K. T. Bioinspired Chiral Inorganic Nanomaterials. *Nat. Rev. Bioeng.* **2023**, 1–19. https://doi.org/10.1038/s44222-022-00014-4.

(5) Kinoshita, S.; Yoshioka, S.; Miyazaki, J. Physics of Structural Colors. *Rep. Prog. Phys.* **2008**, *71* (7), 076401. https://doi.org/10.1088/0034-4885/71/7/076401.

(6) Kinoshita, S.; Yoshioka, S.; Kawagoe, K. Mechanisms of Structural Colour in the Morpho Butterfly: Cooperation of Regularity and Irregularity in an Iridescent Scale. *Proc. R. Soc. Lond. B Biol. Sci.* **2002**, *269* (1499), 1417–1421. https://doi.org/10.1098/rspb.2002.2019.

(7) Wang, Z.; Ding, H.; Liu, D.; Xu, C.; Li, B.; Niu, S.; Li, J.; Liu, L.; Zhao, J.; Zhang, J.; Mu, Z.; Han, Z.; Ren, L. Large-Scale Bio-Inspired Flexible Antireflective Film with Scale-Insensitivity Arrays. *ACS Appl. Mater. Interfaces* **2021**, *13* (19), 23103–23112. https://doi.org/10.1021/acsami.1c02046.

(8) Ingram, A. l; Parker, A. r. A Review of the Diversity and Evolution of Photonic Structures in Butterflies, Incorporating the Work of John Huxley (The Natural History Museum, London from 1961 to 1990). *Philos. Trans. R. Soc. B Biol. Sci.* **2008**, *363* (1502), 2465–2480. https://doi.org/10.1098/rstb.2007.2258.

(9) Hill, G. E.; Hill, G. E.; McGraw, K. J.; McGraw, K. J. *Bird Coloration*; Harvard University Press, 2006.

(10) Christie, J. M.; Murphy, A. S. Shoot Phototropism in Higher Plants: New Light through Old Concepts. *Am. J. Bot.* **2013**, *100* (1), 35–46. https://doi.org/10.3732/ajb.1200340.

(11) Shell, G. S. G.; Lang, A. R. G. Description of Leaf Orientation and Heliotropic Response of Sunflower Using Directional Statistics. *Agric. Meteorol.* **1975**, *15* (1), 33–48. https://doi.org/10.1016/0002-1571(75)90016-3.

(12) Ehleringer, J.; Forseth, I. Solar Tracking by Plants. *Science* **1980**, *210* (4474), 1094–1098. https://doi.org/10.1126/science.210.4474.1094.

(13) Thanisawanyangkura, S.; Sinoquet, H.; Rivet, P.; Cretenet, M.; Jallas, E. Leaf Orientation and Sunlit Leaf Area Distribution in Cotton. *Agric. For. Meteorol.* **1997**, *86* (1), 1–15. https://doi.org/10.1016/S0168-1923(96)02417-3.

(14) Shell, G. S. G.; Lang, A. R. G.; Sale, P. J. M. Quantitative Measures of Leaf Orientation and Heliotropic Response in Sunflower, Bean, Pepper and Cucumber. *Agric. Meteorol.* **1974**, *13* (1), 25–37. https://doi.org/10.1016/0002-1571(74)90062-4.

(15) Garrey, W. E. LIGHT AND THE MUSCLE TONUS OF INSECTS THE HELIOTROPIC MECHANISM. *J. Gen. Physiol.* **1918**, *1* (1), 101–125. https://doi.org/10.1085/jgp.1.1.101.

(16) Loeb, J.; Northrop, J. H. Heliotropic Animals as Photometers on the Basis of the Validity of the Bunsen-Roscoe Law for Heliotropic Reactions. *Proc. Natl. Acad. Sci.* **1917**, *3* (9), 539–544. https://doi.org/10.1073/pnas.3.9.539.

(17) Kaniewska, P.; Campbell, P. R.; Fine, M.; Hoegh-Guldberg, O. Phototropic Growth in a Reef Flat Acroporid Branching Coral Species. *J. Exp. Biol.* **2009**, *212* (5), 662–667. https://doi.org/10.1242/jeb.022624.

(18) Iwase, A.; Sakai, K.; Suzuki, A.; van Woesik, R. Phototropic Adjustment of the Foliaceous Coral Echinopora Lamellosa in Palau. *Estuar. Coast. Shelf Sci.* **2008**, *77* (4), 672–678. https://doi.org/10.1016/j.ecss.2007.10.022.

(19) Tomlinson, P. B. The Structural Biology of Palms. *Struct. Biol. Palms* **1990**.

(20) Datta, B. C. Biologically-Inspired Structural Color: Material Design and Fabrication Strategies Drawn from Nature's Color Palette. Thesis, Massachusetts Institute of Technology, 2021. https://dspace.mit.edu/handle/1721.1/140995 (accessed 2022-04-22).

(21) Li, C.; Liu, Y.; Huang, X.; Jiang, H. Direct Sun-Driven Artificial Heliotropism for Solar Energy Harvesting Based on a Photo-Thermomechanical Liquid-Crystal Elastomer Nanocomposite. *Adv. Funct. Mater.* **2012**, *22* (24), 5166–5174. https://doi.org/10.1002/adfm.201202038.

(22) Deng, J.; Li, J.; Chen, P.; Fang, X.; Sun, X.; Jiang, Y.; Weng, W.; Wang, B.; Peng, H. Tunable Photothermal Actuators Based on a Pre-Programmed Aligned Nanostructure. *J. Am. Chem. Soc.* **2016**, *138* (1), 225–230. https://doi.org/10.1021/jacs.5b10131.

(23) Vassalini, I.; Alessandri, I. "The Phactalysts": Carbon Nanotube/TiO2 Composites as Phototropic Actuators for Wireless Remote Triggering of Chemical Reactions and Catalysis. *Nanoscale* **2017**, *9* (32), 11446–11451. https://doi.org/10.1039/C7NR05104B.

(24) Palagi, S.; Mark, A. G.; Reigh, S. Y.; Melde, K.; Qiu, T.; Zeng, H.; Parmeggiani, C.; Martella, D.; Sanchez-Castillo, A.; Kapernaum, N.; Giesselmann, F.; Wiersma, D. S.; Lauga, E.; Fischer, P. Structured Light Enables Biomimetic Swimming and Versatile Locomotion of Photoresponsive Soft Microrobots. *Nat. Mater.* **2016**, *15* (6), 647–653. https://doi.org/10.1038/nmat4569.

(25) Carim, A. I.; Batara, N. A.; Premkumar, A.; Atwater, H. A.; Lewis, N. S. Self-Optimizing Photoelectrochemical Growth of Nanopatterned Se–Te Films in Response to the Spectral Distribution of Incident Illumination. *Nano Lett.* **2015**, *15* (10), 7071–7076. https://doi.org/10.1021/acs.nanolett.5b03137.

(26) Carim, A. I.; Batara, N. A.; Premkumar, A.; May, R.; Atwater, H. A.; Lewis, N. S. Morphological Expression of the Coherence and Relative Phase of Optical Inputs to the Photoelectrodeposition of Nanopatterned Se–Te Films. *Nano Lett.* **2016**, *16* (5), 2963–2968. https://doi.org/10.1021/acs.nanolett.5b04999.

(27) Carim, A. I.; Batara, N. A.; Premkumar, A.; Atwater, H. A.; Lewis, N. S. Polarization Control of Morphological Pattern Orientation During Light-Mediated Synthesis of Nanostructured Se–Te Films. *ACS Nano* **2016**, *10* (1), 102–111. https://doi.org/10.1021/acsnano.5b05119.

(28) Sadtler, B.; Burgos, S. P.; Batara, N. A.; Beardslee, J. A.; Atwater, H. A.; Lewis, N. S. Phototropic Growth Control of Nanoscale Pattern Formation in Photoelectrodeposited

Se–Te Films. *Proc. Natl. Acad. Sci.* **2013**, *110* (49), 19707–19712. https://doi.org/10.1073/pnas.1315539110.

(29) Hamann, K. R.; Carim, A. I.; Meier, M. C.; Lewis, N. S. Path-Dependent Morphological Evolution of Se–Te Mesostructures Prepared by Inorganic Phototropic Growth. *J. Am. Chem. Soc.* **2020**, *142* (47), 19840–19843. https://doi.org/10.1021/jacs.0c09798.

(30) Hamann, K. R.; Meier, M. C.; Lewis, N. S.; Carim, A. I. Plastic Morphological Response to Spectral Shifts during Inorganic Phototropic Growth. *JACS Au* **2022**, *2* (4), 865–874. https://doi.org/10.1021/jacsau.1c00588.

(31) Simonoff, E.; Muñoz, L. X. V.; Lewis, N. S. Increased Spatial Randomness and Disorder of Nucleates in Dark-Phase Electrodeposition Lead to Increased Spatial Order and Pattern Fidelity in Phototropically Grown Se–Te Electrodeposits. *Nanoscale* **2020**, *12* (44), 22478–22486. https://doi.org/10.1039/D0NR07617A.

(32) Simonoff, E.; Lichterman, M. F.; Papadantonakis, K. M.; Lewis, N. S. Influence of Substrates on the Long-Range Order of Photoelectrodeposited Se–Te Nanostructures. *Nano Lett.* **2019**, *19* (2), 1295–1300. https://doi.org/10.1021/acs.nanolett.8b04891.

(33) Fulop, G. F.; Taylor, R. M. Electrodeposition of Semiconductors. *Annu. Rev. Mater. Sci.* **1985**, *15* (1), 197–210. https://doi.org/10.1146/annurev.ms.15.080185.001213.

(34) Bard, A. J.; Faulkner, L. R.; White, H. S. *Electrochemical Methods: Fundamentals and Applications*; John Wiley & Sons, 2022.

(35) Pourbaix, M. *Atlas of Electrochemical Equilibria in Aqueous Solutions*; National Association of Corrosion Engineers, 1974.

(36) Carim, A. I.; Meier, M. C.; Kennedy, K. M.; Richter, M. H.; Hamann, K. R.; Lewis, N. S. Assessing Effects of Near-Field Synergistic Light Absorption on Ordered Inorganic Phototropic Growth. *J. Am. Chem. Soc.* **2021**, *143* (10), 3693–3696. https://doi.org/10.1021/jacs.0c13085.

(37) Carim, A. I.; Hamann, K. R.; Batara, N. A.; Thompson, J. R.; Atwater, H. A.; Lewis, N. S. Template-Free Synthesis of Periodic Three-Dimensional PbSe Nanostructures via Photoelectrodeposition. *J. Am. Chem. Soc.* **2018**, *140* (21), 6536–6539. https://doi.org/10.1021/jacs.8b02931.

(38) Hamann, K. R.; Carim, A. I.; Meier, M. C.; Thompson, J. R.; Batara, N. A.; Yermolenko, I. S.; Atwater, H. A.; Lewis, N. S. Optically Tunable Mesoscale CdSe Morphologies via Inorganic Phototropic Growth. *J. Mater. Chem. C* **2020**, *8* (36), 12412–12417. https://doi.org/10.1039/D0TC02126A.

(39) Fankhauser, C.; Chory, J. Light Control of Plant Development. *Annu. Rev. Cell Dev. Biol.* **1997**, *13* (1), 203–229. https://doi.org/10.1146/annurev.cellbio.13.1.203.

(40) Whippo, C. W.; Hangarter, R. P. Phototropism: Bending towards Enlightenment. *Plant Cell* **2006**, *18* (5), 1110–1119. https://doi.org/10.1105/tpc.105.039669.

(41) Enders, T. A.; Strader, L. C. Auxin Activity: Past, Present, and Future. *Am. J. Bot.* **2015**, *102* (2), 180–196. https://doi.org/10.3732/ajb.1400285.

(42) Esmon, C. A.; Tinsley, A. G.; Ljung, K.; Sandberg, G.; Hearne, L. B.; Liscum, E. A Gradient of Auxin and Auxin-Dependent Transcription Precedes Tropic Growth Responses. *Proc. Natl. Acad. Sci.* **2006**, *103* (1), 236–241. https://doi.org/10.1073/pnas.0507127103.

(43) Dasog, M.; Carim, A. I.; Yalamanchili, S.; Atwater, H. A.; Lewis, N. S. Profiling Photoinduced Carrier Generation in Semiconductor Microwire Arrays via

Photoelectrochemical Metal Deposition. *Nano Lett.* **2016**, *16* (8), 5015–5021. https://doi.org/10.1021/acs.nanolett.6b01782.

(44) Lanyon, H. P. D. Optical and Electrical Properties of Selenium-Tellurium Alloys. *J. Appl. Phys.* **1964**, *35* (5), 1516–1523. https://doi.org/10.1063/1.1713659.

(45) Xiao, Z.-L.; Han, C. Y.; Kwok, W.-K.; Wang, H.-H.; Welp, U.; Wang, J.; Crabtree, G. W. Tuning the Architecture of Mesostructures by Electrodeposition. *J. Am. Chem. Soc.* **2004**, *126* (8), 2316–2317. https://doi.org/10.1021/ja0315154.

(46) Siegfried, M. J.; Choi, K.-S. Elucidating the Effect of Additives on the Growth and Stability of Cu2O Surfaces via Shape Transformation of Pre-Grown Crystals. *J. Am. Chem. Soc.* **2006**, *128* (32), 10356–10357. https://doi.org/10.1021/ja063574y.

(47) Liu, R.; Vertegel, A. A.; Bohannan, E. W.; Sorenson, T. A.; Switzer, J. A. Epitaxial Electrodeposition of Zinc Oxide Nanopillars on Single-Crystal Gold. *Chem. Mater.* **2001**, *13* (2), 508–512. https://doi.org/10.1021/cm000763l.

(48) Meier, M. C.; Cheng, W.-H.; Atwater, H. A.; Lewis, N. S.; Carim, A. I. Inorganic Phototropism in Electrodeposition of Se–Te. *J. Am. Chem. Soc.* **2019**, *141* (47), 18658–18661. https://doi.org/10.1021/jacs.9b10579.

(49) Iwasa, Y.; Cohen, D.; Leon, J. A. Tree Height and Crown Shape, as Results of Competitive Games. *J. Theor. Biol.* **1985**, *112* (2), 279–297. https://doi.org/10.1016/S0022-5193(85)80288-5.

(50) Farrior, C. E.; Bohlman, S. A.; Hubbell, S.; Pacala, S. W. Dominance of the Suppressed: Power-Law Size Structure in Tropical Forests. *Science* **2016**, *351* (6269), 155–157. https://doi.org/10.1126/science.aad0592.

(51) Chen, S.; Zhang, J.; Jia, P.; Xu, J.; Wang, G.; Xiao, S. Effects of Size Variation and Spatial Structure on Plastic Response of Plant Height to Light Competition. *Chin. Sci. Bull.* **2010**, *55* (12), 1135–1141. https://doi.org/10.1007/s11434-010-0107-5.

(52) Agrawal, A. A. Phenotypic Plasticity in the Interactions and Evolution of Species. *Science* **2001**, *294* (5541), 321–326. https://doi.org/10.1126/science.1060701.

(53) Chen, R.; Rosen, E.; Masson, P. H. Gravitropism in Higher Plants1. *Plant Physiol.* **1999**, *120* (2), 343–350. https://doi.org/10.1104/pp.120.2.343.

(54) Hangarter, R. P. Gravity, Light and Plant Form. *Plant Cell Environ.* **1997**, *20* (6), 796–800. https://doi.org/10.1046/j.1365-3040.1997.d01-124.x.

(55) Johns, J. W.; Yost, J. M.; Nicolle, D.; Igic, B.; Ritter, M. K. Worldwide Hemisphere-Dependent Lean in Cook Pines. *Ecology* **2017**, *98* (9), 2482–2484. https://doi.org/10.1002/ecy.1850.

(56) Horn, H. S. *The Adaptive Geometry of Trees*; Princeton University Press, 1971.

(57) Seidel, D.; Ruzicka, K. J.; Puettmann, K. Canopy Gaps Affect the Shape of Douglas-Fir Crowns in the Western Cascades, Oregon. *For. Ecol. Manag.* **2016**, *363*, 31–38. https://doi.org/10.1016/j.foreco.2015.12.024.

(58) McClain, K. M.; Morris, D. M.; Hills, S. C.; Buse, L. J. The Effects of Initial Spacing on Growth and Crown Development for Planted Northern Conifers: 37-Year Results. *For. Chron.* **1994**, *70* (2), 174–182. https://doi.org/10.5558/tfc70174-2.

(59) Duchemin, L.; Eloy, C.; Badel, E.; Moulia, B. Tree Crowns Grow into Self-Similar Shapes Controlled by Gravity and Light Sensing. *J. R. Soc. Interface* **2018**, *15* (142), 20170976. https://doi.org/10.1098/rsif.2017.0976.

(60) Simonoff, E.; Thompson, J. R.; Meier, M. C.; Kennedy, K. M.; Hamann, K. R.; Lewis, N. S. Preseeded Optical Scatterers as a Template for Enhancing Order in Inorganic Phototropic Growth. *J. Phys. Chem. C* **2021**, *125* (17), 9571–9581. https://doi.org/10.1021/acs.jpcc.1c02746.

(61) Hale, G. M.; Querry, M. R. Optical Constants of Water in the 200-Nm to 200-Mm Wavelength Region. *Appl. Opt.* **1973**, *12* (3), 555–563. https://doi.org/10.1364/AO.12.000555.